Biomaterials Advances 172 (2025) 214249

Contents lists available at ScienceDirect

Biomaterials Advances

journal homepage: www.journals.elsevier.com/materials-science-and-engineering-c

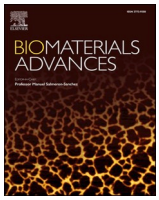

Evaluation of the effects of cartilage decellularized ECM in optimizing PHB-chitosan-HNT/chitosan-ECM core-shell electrospun scaffold: Physicochemical and biological properties

Sepideh Ghadirian, Laleh Shariati, Saeed Karbasi *

Department of Biomaterials and Tissue Engineering, School of Advanced Technologies in Medicine, Isfahan University of Medical Sciences, Isfahan, Iran

ARTICLE INFO

Keywords:
Cartilage decellularized ECM
Polyhydroxybutyrate
Chitosan
Halloysite nanotubes
Core-shell
Electrospun scaffold

ABSTRACT

Cartilage regeneration is still a highly challenging field due to its low self-healing ability. This study used a core-shell electrospinning technique to enhance cartilage tissue engineering by incorporating cartilage extracellular matrix (ECM). The core of fibers included poly(3-hydroxybutyrate)-Chitosan (PHB-Cs) and Halloysite nanotubes. The shell of fibers consisted of Cs and ECM (0, 1, 3, 5 wt%). Subsequently, the scaffolds were named 0E, 1E, 3E, and 5E. The study aimed to assess the impact of ECM on cellular behavior and chondrogenesis. Our findings indicate that ECM reduced fiber diameter from 775 nm for the 0E scaffold to 454 nm for the 1E scaffold. Water contact angle measurements revealed an increasing trend by ECM addition, from 42° for 0E to 67° for 1E. According to mechanical analysis, the 1E scaffold represented the highest strength (5.81 MPa) and strain (3.17%). Based on these analyses, the 1E was considered the optimum scaffold. MTT analysis showed cell viability of over 80% for the 0E and 1E. Also, the gene expression level was assessed for *Collagen II*, *Aggrecan*, *SOX 9*, and *Collagen X*. The results represented that in the 1E scaffold *Collagen II*, Aggrecan, and *SOX 9* were more upregulated at the end of the 21st day. However, in the 1E scaffold *collagen X,* as a hypertrophy marker, was downregulated at the end of the experiment. Overall, these results confirmed the potential of the 1E scaffold to be introduced as a promising cartilage tissue engineering scaffold for further studies.

1. Introduction

Cartilage tissue has a limited capacity for self-repair which is mainly due to its intrinsic avascular nature and low cellularity. Cartilage contains few chondrocytes and progenitor cells that help tissue repair and regeneration. Additionally, cartilage lacks blood vessels, nerves, and lymph channels. The sparse vascular structures limit obtaining circulating repair cells and nutrients that are necessary for regeneration. Consequently, the combination of these features results in a poor self-healing process [1,2]. On the other hand, the growing elderly population worldwide means that the population of patients with cartilage damage is increasing. Conventional treatments like chondroplasty and microfractures can treat cartilage defects but cannot completely restore full function [3].

Tissue engineering which has emerged since 1977 offers an alternative technique to overcome the limitations of traditional clinical therapies of cartilage defects. In this approach, a combination of porous scaffold, living cells, and bioenvironmental factors is used to stimulate the formation of new tissue [1]. The ultimate goal is to regenerate cartilage at the defect site and restore the structural, and functional properties of the native tissue [4].

Scaffolds in tissue engineering, provide porous templates for cell attachment and biophysical cues to organize tissue growth. Various techniques have been applied to fabricate scaffolds with customized architectures and to have the most similarity with the target tissue [5,116]. Electrospinning has emerged as one of the most versatile and widely used methods to fabricate scaffolds from fibers. In the Electrospinning technique, polymer fibers are produced in different ranges from nano to micro-scale [6–8]. The advantages of electrospinning like ease, cost-effectiveness, and versatility have made this technology so functional for different tissue regeneration from skin to cartilage and blood vessels [6,9–13]. Electrospinning has the potential for fabricating fibers in different architectures, such as solid fibers, hollow fibers, core-shell fibers, and aligned fibers versus random nonwoven meshes. Among these, core-shell fibers fabricated through coaxial electrospinning have attracted particular interest [14].

* Corresponding author.
E-mail address: karbasi@med.mui.ac.ir (S. Karbasi).

https://doi.org/10.1016/j.bioadv.2025.214249
Received 3 January 2025; Received in revised form 9 February 2025; Accepted 25 February 2025
Available online 28 February 2025

Core-shell electrospinning is a specialized technique that produces fibers from two distinct polymer compositions layered in a core-shell fashion. This is achieved through simultaneous electrospinning of two different polymer solutions that do not mix because of differences in properties like viscosity [15,16]. Core-shell fibers can also be produced through phase separation during the electrospinning of immiscible polymers [17]. Core-shell electrospun fibers can mimic the fibrous architecture of native cartilage in different aspects. By selecting biocompatible polymers and extracellular matrix (ECM)-based materials in the shell can provide an environment that simulates the native matrix and promotes cell-material interactions. On the other hand, the core can be designed to reinforce mechanical strength. This engineered design helps to preserve structural integrity under physiological loads. Core and shell also have the potential for controlled release of bioactive components with distinct release kinetics according to different healing stages [18–21]. Similarly, in a study by Baek et al. [21] co-axial electrospinning was used for meniscus tissue engineering. They generate core-shell nanofibers with a core of polylactic acid to mimic mechanical strength and a shell of collagen to enhance cell attachment and matrix synthesis. According to their results, co-axial electrospun scaffolds had greater mechanical properties than collagen scaffolds. Also, SEM and confocal images revealed that cells seeded on core-shell scaffolds attached to the entire surface of the fibers. These findings confirmed the hypothesis that a shell of collagen increases cell attachment. In another study by Yin et al. [22] coaxial electrospinning was applied for tracheal cartilage tissue engineering. The authors used poly (L-lactic acid-*co*-caprolactone)/collagen combination as the shell and kartogenin solution as the core. This structure allowed for the controlled release of kartogenin over an extended period. The scaffold also demonstrates good biocompatibility, indicated by the proliferation and morphology of mesenchymal stem cells cultured on it. Also, the results of RT-PCR evaluation confirmed the effectiveness of this structure in chondrogenic differentiation of bone marrow mesenchymal stem cells cultured on the core-shell nanofibrous scaffold.

In particular, a wide range of polymers are spinnable. Synthetic polymers like poly (lactic acid) (PLA), poly (glycolic acid) (PGA), polycaprolactone (PCL), poly (lactic-co-glycolic acid) (PLGA), poly (vinyl alcohol) (PVA), and poly(3-hydroxybutyrate) (PHB) have been successfully electrospun. Features like favorable viscosity, charge density, molecular weight, and solubility attributes make these polymers appropriate options for fabricating smooth fiber [23].

PHB is a synthetic polymer from the polyhydroxyalkanoates (PHA) family and is known in tissue engineering applications due to its suitable mechanical properties, biocompatibility, non-toxic degradation products, piezoelectricity, and excellent spinnability [24]. However, its intrinsic brittleness, hydrophobicity, and high crystallinity motivate researchers to combine it with natural polymers like Cs [25], keratin [26], and starch [27]. This approach helps to compensate for PHB limitations and also modifies the degradation profile [25]. Cs is a polysaccharide originating from chitin that offers hydrophilicity and bioactive properties including antibacterial activity, biocompatibility, and hemostatic functions [28–30]. Combining these two polymers for electrospinning leads to the construction of scaffolds with improved hydrophilicity, degradation profile, and cell adhesion properties compared to PHB alone [25,31–34]. On the other hand, this approach decreases the mechanical properties of the final scaffold required for load-bearing tissues like cartilage. In the literature, applying nanostructures is a successful strategy to improve the mechanical properties of scaffolds [35]. The nanostructures like alumina nanowires, nano clays, carbon nanotubes, bioglass nanoparticles, and cellulose nanofibers integrate within the polymer matrix, enhancing constructs' overall mechanical properties like tensile strength [25,26,36–39].

Halloysite is an aluminosilicate nanotubular clay, that is recently used for reinforcing polymer scaffolds. It has a positively charged inner lumen and a negatively charged outer surface [40]. In our previous study, HNTs were applied to strengthen electrospun PHB-Cs scaffolds. HNTs made interfacial bonding with the polymer matrix and enhanced scaffold tensile strength compared to PHB-Cs alone. The study demonstrated that the PHB-Cs composite containing 3 wt% HNTs could serve as a promising alternative for tissue engineering scaffolds, offering improved structural and functional properties [33]. In the present study, to leverage the properties of the PHB- Cs /HNT fibers, this combination was selected for the core layer of core-shell fibers. Following that, the appropriate selection of materials for the shell layer can result in improved cellular behaviors in terms of cellular adhesion, proliferation, and even differentiation. The core-shell fiber's structure allows the pairing of this reinforced core with a bioactive shell that mimics the cartilage ECM. The shell layer additionally permits the delivery of growth factors, drugs, and biological compounds to direct cell differentiation and tissue maturation [41].

In this context, decellularized ECM derived from cartilage is emerging as a promising biomaterial for cartilage tissue engineering. ECM is a complex network of proteins and carbohydrates like collagen, fibronectin, elastin, laminin, and glycosaminoglycans (GAG). ECM acts as a structural support and regulates cellular behavior within tissues. Cartilage ECM also has bioactive molecules that can stimulate cartilage regeneration [42–44]. Some studies show the synergy of ECM and Cs in improving the cell behavior of chondrocytes and increasing chondrogenesis. Considering these, the combination of Cs and cartilage decellular ECM can be an ideal option to be used in the fibers' shell [43,45]. I-Chan Lin et al. [46] conducted a study on a chitosan (Cs)-cartilage ECM scaffold to promote chondrogenic differentiation of adipose-derived stem cells (ASCs). According to their results mixing cartilage ECM with Cs significantly improved ASC proliferation compared to pure Cs films. Additionally, they reported ASC spheroid formation within the Cs-cartilage ECM scaffold, which was attributed to enhanced chondrogenic differentiation of the seeded ASCs. Researchers have also used ECM components to improve Cs scaffold characteristics. Choi et al. [47], investigated the effect of collagen type II (Col II) and chondroitin sulfate addition to an injectable Cs hydrogel scaffold. The results showed that the incorporation of Col II and chondroitin sulfate into the Cs hydrogels increased chondrogenesis. Also, the presence of Col II significantly improved cellular condensation within the hydrogels. These improvements were attributed to the integrin α10 binding to Col II, leading to increased cell-matrix adhesion.

Furthermore, many studies, have investigated the advantages of ECM incorporation on cellular behavior in polymer scaffolds regardless of Cs presence. For example, a study conducted by Asghari et al. [48] considered the effect of 1, 2, and 3 wt% ECM on PHB electrospun scaffolds. According to the findings, the samples containing 3 wt% ECM had the highest level of cellular viability. This improvement was correlated to increased hydrophilicity and higher amount of ECM protein in the scaffold structure.

The present study is about fabricating a novel tissue engineering scaffold by the core-shell electrospinning technique. According to the authors' previous study, the combination of PHB-Cs/HNT was used in the core of fibers [33]. For the shell, a combination of Cs and ECM was applied. It was hypothesized that the ECM incorporation in the shell can improve cellular behavior and chondrogenesis. This investigation aimed to evaluate the impact of ECM on the physical, mechanical, and biological properties of the scaffolds.

2. Experimental

2.1. Material

The poly(3-hydroxybutyrate) (PHB), chitosan (Cs), and halloysite nanotubes (HNTs) used in this study were purchased from Sigma Aldrich (USA). Trifluoroacetic acid (TFA) was obtained from Carlo Erba company (France). Phosphate-buffered saline (PBS) was acquired from Ceram Razi Co. (Iran). Cell culture materials including Dulbecco's Modified Eagle Medium-F12 (DMEM-F12), fetal bovine serum (FBS),

penicillin/streptomycin, as well as methyl thiazolyldiphenyl-tetrazolium bromide (MTT) and trypsin-ethylenediaminetetraacetic acid (EDTA) were purchased from Sigma-Aldrich (USA). Fixatives glutaraldehyde and dimethyl sulfoxide (DMSO) were obtained from Sigma-Aldrich (USA) and Merck (Germany), respectively.

2.2. Decellularization of cartilage ECM

The decellularization process was performed following the protocol established in our previous study [48]. Articular cartilage samples were harvested from the femur and tibia condyle regions of bovine knee joints. The bovine joints were collected from a local abattoir after slaughter and brought to the laboratory for cartilage separation. The cartilage sections were at first cleaned and parted into smaller pieces. Then these pieces were soaked in PBS with 2 % penicillin-streptomycin under sterile conditions for 30 min. The rinsed cartilage slices were then lyophilized for 48 h at −50 °C. In the next step, the lyophilized tissues freeze-milled into a powder. The milled cartilage was agitated in 2 % sodium dodecyl sulfate (SDS) solution for 5 h followed by 4 % SDS for 3 h. The SDS solutions were evacuated and the remaining ECM was rinsed with PBS twice for 5–10 min each time. After a third 24 h PBS rinse with shaking, the suspension was centrifuged and the sedimented ECM was lyophilized for 24 h again to obtain decellularized cartilage ECM powder [48–50].

2.3. Enzymatic solubilization of decellularized ECM

Enzymatic cleavage by pepsin is a conventional technique to produce solubilized ECM. In this work, the cartilage ECM powder was solubilized based on a protocol reported by Freytes et al. [51]. The ECM powder was mixed with 0.1 M hydrochloric acid (HCl) at 10 mg/ml and pepsin was added to a final concentration of 1 mg/ml. This solution was agitated at room temperature for 48 h, during this period pepsin digested and solubilized the ECM. After solubilization, 1 M sodium hydroxide (NaOH) was added in order to neutralize the pH to the physiological level. Finally, the solubilized ECM was centrifuged at 1800 rpm for 5 min and after that lyophilized for 48 h to prepare it for use [48,51]. Throughout the article, the solubilized decellularized ECM is abbreviated as ECM.

2.4. ECM biochemical analysis

ECM biochemical analysis, including DNA, GAG, and collagen content measurement is necessary to verify the ECM decellularization process. For DNA content analysis, it is necessary to digest the samples in Tris-EDTA buffer solution containing proteinase K (1 mg/ml), iodoacetamide (1 μg/ml), and pepstatin A (18.5 μg/ml). The digestion process lasted for 24 h at 65 °C. Then a DNA assay kit was used to measure the DNA content according to the manufacturer's instructions. The sample absorbance was measured using a spectrofluorometer (PerkinElmer LS50B) at 480/520 nm which belong to excitation/emission wavelengths. The DNA concentration was determined by interpolation against a standard curve of double-stranded DNA [52].

GAG content is usually quantified by using a dimethyl methylene blue (DMMB) dye solution. For this purpose, DMMB dye was prepared at a PBE buffer involving Na2EDTA (3.72 g/l) and Na_2HPO_4 (14.2 g/l) with a pH of 6.5. The sample's absorbance was read at the wavelength of 520 nm by a multi-well plate reader (BioTek Synergy H1). The GAG concentration was calculated by comparing absorbance readings against the chondroitin sulfate standard curve [52,53].

Hydroxyproline is an abundant amino acid in collagen structure that acts as a biomarker for collagen content as well. For evaluating the hydroxyproline of the samples, a commercial Hydroxyproline assay kit was used. 10 mg of lyophilized sample was digested in 100 μl of hydrochloric acid (12 mol/l) at a temperature of 120 °C for 3 h. After that, sodium hydroxide was used to neutralize the solution to pH 6–7. In the next step, the samples were centrifuged to remove debris. The supernatant was collected in new tubes. In order to initiate oxidation reaction Chloramine-T reagent was added to samples and incubated at room temperature for 5 mins. The chromophore (color-producing reaction) was developed by adding *p*-dimethylaminobenzaldehyde (DMAB) solution and incubating at 60 °C for 90 min. The absorbance of the samples was measured by a multi-well plate reader at the wavelength of 520 nm. The hydroxyproline concentration in each sample was measured by extrapolating the absorbance values against a hydroxyproline standard curve [52,53].

2.5. Preparation of core-shell electrospun scaffolds

According to protocols from previous studies [25,33], the fiber core solution was prepared as follows. First, 9 wt% of PHB was dissolved in TFA solvent at 45 °C. Next, 20 wt% Cs was added to the PHB/TFA solution. The temperature was increased to 60 °C to dissolve the Cs, and the mixture was stirred for 1 h. Then, 3 wt% HNT were sonicated in an appropriate amount of TFA using a probe sonicator to obtain a uniform nanoparticle suspension. This suspension was added to the polymer solution. After mixing for 15 min, the core solution was ready for electrospinning.

For the shell solution, 4 wt% Cs was dissolved in a 90:10 TFA/acetic acid solvent mixture for 1 h at 60 °C. The solvent proportions were according to previous reports [54]. Then 0, 1, 3, and 5 wt% of the prepared ECM were added to the Cs cooled solution at room temperature. This mixture was stirred for 30 min. Finally, the core and shell solutions were drawn up into separate 1 cc syringes. Then the syringes were connected to the inlets of a coaxial core-shell electrospinning nozzle. This nozzle contains two inlets that allow for the simultaneous spinning of the core and shell solution. The assembled core-shell nozzle was then embedded in the electrospinning apparatus. The distance between the nozzle tip to the constant collector was 15 cm and the applied voltage was 20 Kv. Also, the feed rate of the core and shell solution was 0.006 and 0.004 ml/min respectively. These parameters setting led to the formation of one straight Taylor cone at the nozzle tip and avoided separate cones for the core and shell. The deposited meshes were separated from the collector and punched into dimensions appropriate for different analyses according to the relevant standards. The scaffolds' thickness remained approximately constant at around 0.05 mm.

Table 1 outlines the abbreviations used to name the various scaffold groups prepared through the core-shell electrospinning process. As shown, the variable component between the scaffolds is the amount of ECM in the shell layer.

To characterize the electrospun scaffolds, initial evaluations were conducted on all groups, including scanning electron microscopy (SEM), hydrophilicity assessments, and mechanical testing. Based on these results, the optimal scaffold was selected for further analysis. Subsequent comparisons were made between this ECM-containing scaffold and the control group without ECM (0E).

2.6. Evaluation of scaffold's morphology

2.6.1. SEM imaging

To measure and compare the fiber diameter and porosity of the electrospun scaffolds, SEM was conducted on all groups (LEO 1430 VP, Germany). Before imaging, the samples were coated with a thin layer of gold, and images were captured in two different magnifications (2500×,

Table 1
Abbreviations used for core-shell electrospun scaffolds.

Terms	Abbreviations
PHB-Cs-HNT/Cs	0E
PHB-Cs-HNT/Cs-ECM (1 wt%)	1E
PHB-Cs-HNT/Cs-ECM (3 wt%)	3E
PHB-Cs-HNT/Cs-ECM (5 wt%)	5E

and 5000×). The SEM images were further analyzed by ImageJ software (NIH, USA) to calculate the average fiber diameters and standard deviation. For this purpose, 30 fibers were selected randomly and analyzed in each group. The porosity percentage of samples was also determined by using MATLAB software (R2016a). This method for evaluating porosity has been verified by various studies [55].

2.6.2. Atomic force microscopy (AFM)

To measure the surface roughness of electrospun scaffolds AFM was utilized. For imaging, a 15 × 15 μm^2 surface area was scanned. Roughness analysis was quantified by measuring 3 key parameters including R_a, R_q, and R_z values for each scaffold sample. R_a indicates the arithmetic mean of the surface profile heights, R_q is the root-mean-square average of the profile heights, and R_z is the average height of the five tallest peaks and five deepest valleys.

2.6.3. Transmission Electron Microscopy (TEM)

TEM imaging was conducted to verify the formation of the core-shell structure. Before spinning, a copper grid was attached to the apparatus collector. Subsequently, electrospun fibers were deposited on the grid surface. After electrospinning, the grid was detached and coated. The grid was then transformed into the TEM microscope to apply imaging (Philips EM 208 S TEM /Netherlands).

2.6.4. Energy-dispersive X-ray spectroscopy (EDS) analysis

To verify the HNT loading inside the fiber through elemental analysis, EDS was applied. EDS analysis was conducted using a SEM equipped with an EDX detector. For HNT determination, Characteristic peaks for aluminum (1.487 keV) and silicon (1.740 keV) were scanned [56].

2.7. Fourier transform infrared spectroscopy (FTIR)

FTIR spectroscopy is a usual technique for identifying chemical compounds and functional groups. Studying and comparing FTIR peaks can assess the incorporation of ECM and other components in the scaffold. For this, spectroscopy was applied to the ECM and scaffolds over the range of 4000 to 400 cm^{-1} (Bruker FTIR device /Karlsruhe, Germany).

2.8. Raman spectroscopy

Raman spectral patterns can be used to identify chemical bonds and molecular structures. In many studies, biological tissues and compounds were characterized using Raman spectroscopy. Raman analysis was carried out on ECM, 0E, and 1E scaffolds to investigate the ECM effects in the scaffold structure and analyze the formed bonds. The tests were carried out using a Raman system (Teksan N1541, Iran) equipped with a 543 nm laser source providing approximately 60 mW power.

2.9. Differential Scanning Calorimetry (DSC)

DSC was conducted to determine changes in thermal characteristics and crystallinity of the electrospun scaffolds after ECM incorporation. Analysis was performed under a nitrogen environment (DSC131 Evo calorimeter/France). Samples were heated from 27 °C to 200 °C at a constant rate of 10 °C/min. The primary polymer component (PHB) shows a melting endotherm peak that allows for quantification of its crystallinity percent before and after ECM integration.

The degree of PHB crystallinity (χ_c) was calculated using Eq. (1). Here the measured melting enthalpy (ΔH_m), the enthalpy of fully crystalline PHB (ΔH_m°), which is a known value of 146 J/g, and PHB mass fraction (Φ_{PHB}) are necessary to calculate χ_c:

$$X_C = \frac{\Delta H_m / \phi_{PHB}}{\Delta H_m^\circ} \quad (1)$$

2.10. Analysis of surface hydrophilicity

To assess surface hydrophilicity, water contact angles of the electrospun scaffolds were measured (XCA-50, Iran). Scaffolds were punched into rectangular pieces (2 × 5 cm^2). Drops of purified water (4 μl) were gently deposited on each scaffold surface at the appropriate distances ($n = 3$). Images were captured at the 10th second after drop deposition. Finally, captured images were processed for contact angle calculation by Image J software.

2.11. Mechanical characterization

The mechanical properties of the electrospun scaffolds were evaluated by tensile testing (Zwick Roell, Germany). This analysis was conducted based on ASTM D882 guidelines (n = 3). Accordingly, rectangular samples (30 × 10 mm^2) were cut, and thickness was precisely measured for each sample via a micrometer. The samples were attached to the apparatus grips and underwent uniaxial stretching until failure. The load cell and rate of stretching were 20 N and 10 mm/min respectively. Stress-strain curves were drawn by plotting the measured force against elongation.

2.12. In vitro degradation

The biodegradation profiles of the electrospun scaffolds were evaluated by recording mass loss over time according to ASTM protocol F1635. Scaffolds were punched into 1 × 1 cm^2 and the initial dry mass (M_1) was recorded. Samples were then immersed in 5 ml of PBS (pH = 7.4) at 37 °C. At specific time intervals through 100 days, the scaffold pieces were extracted from PBS and rinsed in purified water. Then scaffolds were dried for 4 h at 37 °C before weighing to determine a final dry mass (M_0). The percent of weight loss was calculated through the Eq. (2):

$$\textit{weight loss}\% = \frac{m_1 - m_0}{m_1} \times 100 \quad (2)$$

Additionally, pH measurements were conducted on the PBS solutions throughout scaffold incubation to realize media pH changes. Finally, FTIR analysis and SEM imaging were repeated on samples after the 100-day interval to confirm chemical and morphological changes induced through PBS exposure.

2.13. Cellular behavior assay

2.13.1. Cell culture

For *in vitro* analysis, human costal chondrocytes (Pasteur Institute of Iran/NCBI code: C620, Designation: C28/I2) were used. Cells were preserved in DMEM-F12 media containing 10 % fetal bovine serum and 1 % penicillin/streptomycin (37 °C, and 5 % CO_2). When cells' confluency reached about 80 %, cell passaging was applied. To separate adherent cells, trypsin/EDTA (0.25 %) was used. Before cell seeding, the scaffolds were punched into circular forms with 0.7 cm diameter. Then scaffolds were sterilized through 3 steps: washing with PBS, immersion in ethanol for 30 min, and UV exposure for 30 min.

For cell attachment and MTT analysis, scaffolds were placed in 24-well plates and chondrocytes were seeded on the scaffolds at a density of 2 × 10^4 cells per well. Then scaffolds were incubated for 7 days and the media was changed every 48 h.

2.13.2. Cell attachment

Cell adhesion and spreading on the scaffolds were evaluated by SEM imaging. For this, seeded scaffolds were rinsed by PBS, and then fixed for 30 min in 4 % glutaraldehyde. After fixation, scaffolds were washed again. In the next step, scaffolds were dehydrated through graded alcohol solutions from 50 % to 100 % ethanol. Samples were coated

before imaging via SEM.

2.13.3. Cell viability

Cellular viability was evaluated by MTT analysis in the 1st, 3rd and 7th days after cell seeding on scaffolds. For this purpose, at each time point, the medium was eliminated and 400 μl of low-glucose DMEM, and 100 μl of MTT solution were added to the scaffold in 24-well plates. After incubation for 4 h at 37 °C, the MTT solution was removed and DMSO was added to extract formazan crystals. After that, 100 μl from each well (dissolved formazan solution) was transferred to a 96-well plate. To measure the optical density of each sample an Elisa plate reader (680, Bio-Rad, Hercules, CA/ USA) was used at the wavelength of 570 nm.

2.13.4. DAPI staining

DAPI staining helps to visualize the nucleus of cells on the scaffolds. For this, the culture medium was removed and the scaffolds were rinsed with PBS. After that, the scaffolds were incubated with 4 % paraformaldehyde solution for 30 min. Then scaffolds were stained with DAPI solution for 1 min. After washing with PBS, the scaffolds were placed under a fluorescent microscope (Olympus BX51) to visualize the nuclei of fixed cells [57].

2.13.5. Gene expression analysis

The role of ECM and scaffold structure on the cartilage gene expression of chondrocytes was evaluated through real-time reverse transcription-quantitative polymerase chain reaction (qRT-PCR). The genes of interest were *collagen II (COL II), collagen X (COL X), SRY-box transcription factor 9 (SOX 9)*, and *aggrecan (AGC)*. At first, chondrocytes were cultured on core-shell scaffolds (0E and 1E) at a 5×10^3 cells/cm^2 concentration. The experiment was applied on 7, 14, and 21 days. Then, total RNA was isolated from each scaffold using a commercial extraction kit (Parstous, Iran). RNA concentration was measured with a Nanodrop spectrophotometer. Subsequently, the RNA was reverse-transcribed to cDNA by an iScript cDNA Synthesis kit (BioRad, US) according to the manufacturer's protocol. Real-time qRT-PCR was performed to quantify RNA using specific primers (Table 2). The thermal cycling conditions consisted of an initial denaturation step at 95 °C for 10 min, followed by 40 cycles of 95 °C for 10 s and 60 °C for 10 s. Relative gene expression was calculated using the $2^{-\Delta\Delta Ct}$ method [24]. The *β-actin* gene served as the housekeeping gene. Gene expression levels were measured relative to the *Beta-actin*. After calculation, final values were reported as fold changes.

2.14. Statistical analysis

All experimental analyses were conducted in triplicate to ensure statistical robustness, with results expressed as mean values ± standard deviation (SD). Statistical analyses were performed using GraphPad Prism 9 software (La Jolla, CA, USA). To evaluate the statistical significance of differences between experimental groups, two-way analysis of variance (ANOVA) was employed. Statistical significance levels were denoted as follows: *$p < 0.05$, **$p < 0.01$, ***$p < 0.001$, and ****$p < 0.0001$.

Table 2
The sequence of primers used for qRT-PCR: *COL II*, *COLX*, *SOX9,* and *AGC*.

Targets genes	Primer sequences (F = forward, R = reverse)
Collagen type X alpha 1 chain	F: TCCCAGCACGCAGAATC R: AACTGTGTCTTGGTGTTGGG
Aggrecan (AGC)	F: ACACCCCATGCAATTTGAG R: GTTTGTAGGTGGTGGCTGTG
Collagen type II (COL2A1)	F: CTGGAAAAGCTGGTGAAAG R: GGAACCACTCTCACCCTTC
Sox9	F: AGCTCTGGAGACTTCTGAACG R: CGTTCTTCACCGACTTCCTC
Beta-actin	F: TTCGAGCAAGAGATGGCCA R: CACAGGACTCCATGCCCAG

3. Results and discussion

3.1. ECM biochemical analysis

During the ECM decellularization process, the cells must be removed while ECM proteins and contents like collagen and GAG are preserved. DNA, GAG, and collagen contents should be assessed before and after decellularization to evaluate decellularization efficacy. DNA content is important since indicates cell removal level and ensures low risk of immunogenicity. While recent research on porcine ECM-derived biomaterials shows that residual DNA might not significantly affect immunological safety, further studies still are needed for bovine and human ECM [58]. In the present study, DNA content was measured using an assay kit as explained in the methods section. As shown in Fig. 1, the decellularization significantly reduced DNA level ($p < 0.05$). Also, the residual DNA concentration was below 50 ng/mg. This level is reported as the threshold in the literature to minimize the risk of adverse host reactions.

According to Fig. 1, GAG and collagen content were also reduced to 60 % and 40 % after decellularization ($p < 0.0001$). While these results express all contents have decreased, it is generally presenting successful decellularization as it suggests the effective removal of cellular components (DNA) while the essential ECM components are still preserved. The literature suggests that the typically lower retention of GAGs compared to collagen is attributed to its higher solubility and smaller molecular size [59,60].

3.2. Evaluation of scaffolds morphology

3.2.1. SEM

SEM images were captured from all groups to assess the morphology and measure the fiber diameter of electrospun scaffolds (Fig. 2). Fig. 2 also shows the histogram of fiber diameter to represent the diameter diversity in each sample. In Fig. 3, the bar charts of mean diameter were plotted to compare all groups and determine whether ECM addition significantly affects the fiber diameter.

As observed in Fig. 3, the addition of ECM to the shell layer resulted in a noticeable reduction in fiber diameter compared to fibers without ECM. The average diameter of the 0E group was 775 ± 330 nm. Incorporating ECM decreased this average down to 454 ± 120 nm, representing a significant difference ($p < 0.05$). This reduction can be attributed to the interactions between ECM components and Cs chains. These interactions may disrupt intrinsic Cs hydrogen bonding and decrease viscosity which may result in fiber thinning during electrospinning [54,61,62]. ECM is a complex of proteins and other biomolecules. Incorporation of ECM into Cs electrospinning solution can alter viscosity and spinnability, consequently affecting the diameter of the fibers [63,64]. Additionally, interfacial bonding between the two

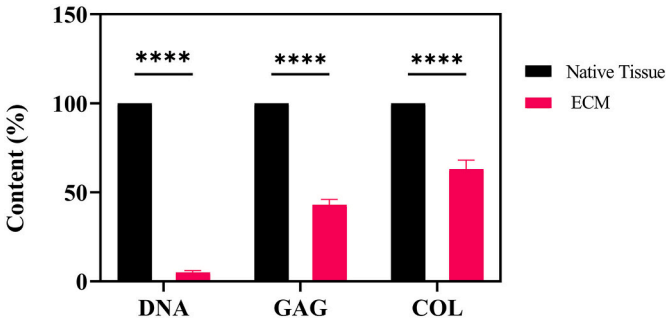

Fig. 1. DNA, GAG, and collagen content of native tissue and decellularized ECM (*****p < 0.0001*).

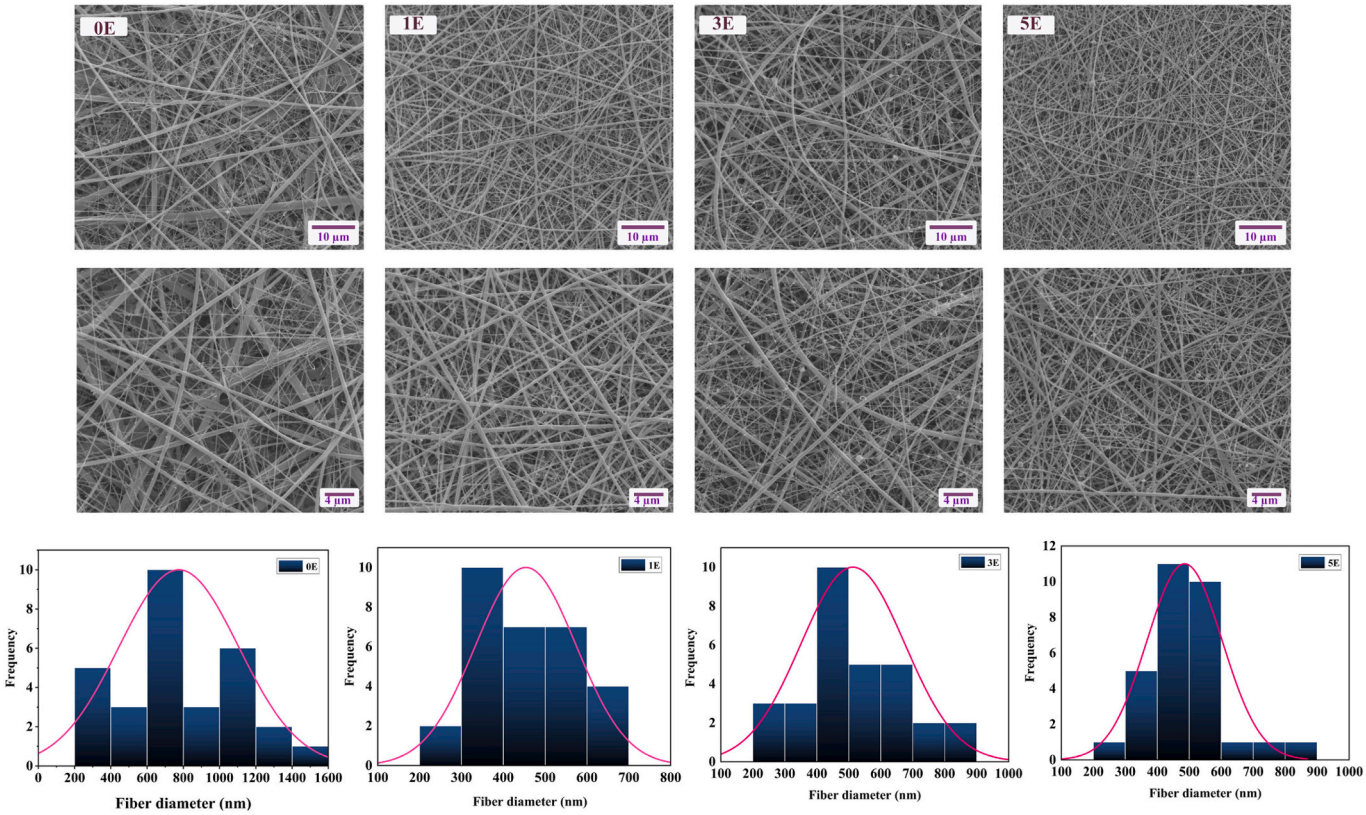

Fig. 2. SEM micrograph and histogram of core-shell electrospun scaffolds (2500×, 5000×).

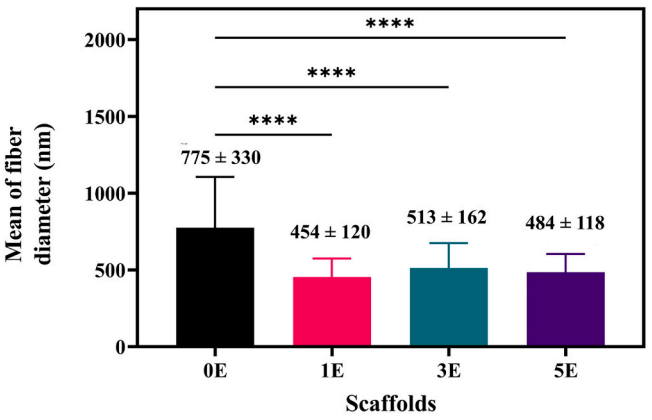

Fig. 3. The average fiber diameter of the scaffolds (**** $p < 0.0001$).

phases may affect viscosity and surface charge at the electrospinning nozzle tip, where the core and shell solutions reach to form the Taylor cone. In coaxial electrospinning, the interface between the core and shell solutions can exhibit various types of bonding depending on the materials and process conditions: physical bonding occurs when the core and shell have similar properties like surface tension or viscosity, that cause adhesion. Electrostatic bonding occurs when the core and shell have opposite charges. Hydrogen bonding can also form between the core and shell polymers, as mentioned in different studies. The interface and bonding interactions are affected by ECM incorporation. In fact, ECM presence modifies the electrostatic environment at the electrospinning nozzle [65–69]. These rheological and electrostatic changes can affect the fiber diameter during jet thinning [69,70]. Here, the addition of ECM to the scaffolds significantly reduced fiber diameter compared to scaffolds without ECM. However, there were no significant differences in fiber diameter among the scaffolds containing ECM. Increasing the percentage of ECM did not produce any consistent trend in fiber diameter for 1E, 3E, and 5E groups. Qualitative analysis of SEM images revealed more uniform fiber distribution in 1E scaffolds compared to the other groups. The histogram data confirmed this finding, which showed the absence of fibers exceeding 700 nm in the 1E group (Fig. 2). On the other hand, approximately 50 %, 13 %, and 6.6 % of fibers in the 0E, 3E, and 5E groups, were thicker than 700 nm.

The porosity of the scaffolds was calculated using MATLAB software and reported in Table 3. The 0E scaffold displayed greater porosity which can be attributed to its heterogeneous fiber diameters and larger average diameters. Incorporating ECM led to thinner diameters, and decreased porosity [71]. However, all core-shell scaffolds still exhibited porosity above 80 %, which is in the optimal range [33]. Analysis of second and third-layers porosities is important because indicates interconnectivity. Interconnected pores are essential for nutrient diffusion, waste removal, and cell infiltration [72]. Porosities of the 0E, 1E, and 5E scaffolds were above 40 % and 20 % for the second and third layers [11].

3.2.2. AFM

AFM was utilized to analyze the surface roughness of the 0E and 1E scaffolds. Fig. 4 illustrates the 3D topographical maps that show surface texture with peaks and valleys for both scaffolds in a 15 × 15 μm^2 area. Map related to the 1E scaffold shows a more irregular surface with

Table 3
Porosity percentage of the scaffolds.

Scaffolds	Porosity (%)		
	First layer	Second layer	Third layer
0E	88 %	50 %	24 %
1E	82 %	42 %	22 %
3E	84 %	44 %	18 %
5E	81 %	42 %	20 %

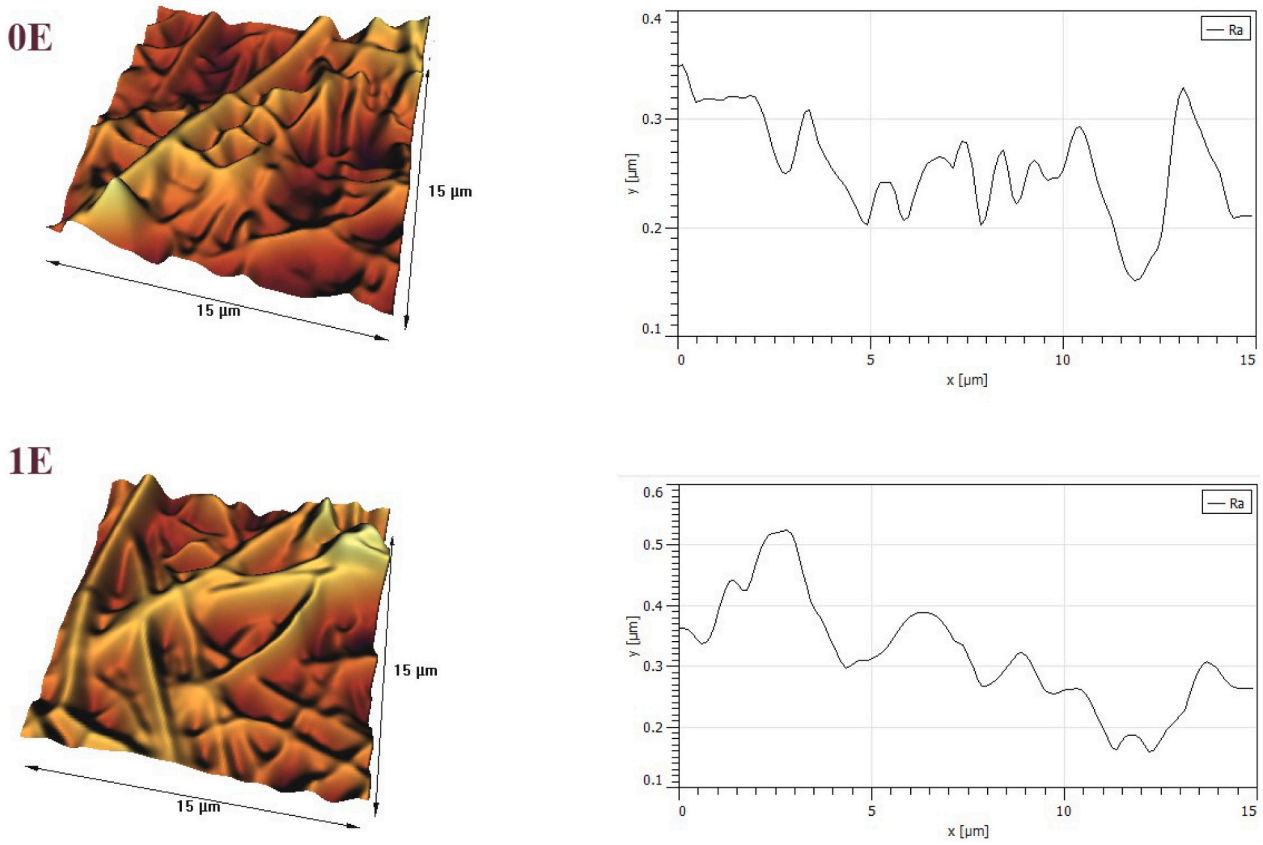

Fig. 4. AFM images of 0E and 1E scaffolds.

sharper peaks and deeper valleys. Also, the line graph in Fig. 4 is related to surface roughness (R_a) over the same area (R_q and R_z line graphs are represented in Figs. S1 and S2). For the 0E sample, the R_a value is <0.4 µm and for the 1E scaffold, R_a reaches approximately 0.5 µm. Quantitative measurements of the R_a, R_q, and R_z are presented in Table 4. These values indicate that ECM incorporation increased overall surface roughness parameters compared to the scaffold without ECM. The greater roughness arises from the introduction of ECM, which enhances nanoscale topographical features on the fiber surfaces. In fact, the addition of ECM altered the core-shell fiber morphology and diameter distribution and increased the surface unevenness [73].

In a specific section of a study conducted by Saberi et al. [74], the effect of cartilage ECM incorporation on the surface roughness of the CS-PEO nanofiber was analyzed. The results revealed that ECM addition (1.17 % wt.) increased parameter R_a from 238 µm to 314 µm. This result confirms our finding and indicates that ECM introduction to the electrospun solution can change the surface roughness.

Surface nanotopography in the form of features like nodes, pits, and protrusions can modulate cell behavior and functions without inducing directional alignment, unlike designed topographic cues. Instead, isotropic and random nanotextures can provide contact guidance through mechanisms that are not still clear [75]. Electrospun scaffolds with random fiber orientations can mimic native ECM and provide nanoscale cues. In the present study, incorporating ECM components into the shell layer increased surface roughness and nanoscale texture.

Table 4
Quantitative measurements of the R_a, R_q, and R_z from AFM analysis for 0E and 1E scaffolds.

Sample	R_a (nm)	R_q (nm)	R_z (nm)
0E	256 ± 45	320 ± 52	708 ± 144
1E	319 ± 90	379 ± 112	895 ± 221

There is some evidence that nanotextured surface cues can improve cell adhesion and functions like proliferation and differentiation compared to smooth surfaces [73,75,76]. It is proposed that nanotopography changes interfacial forces and subsequently alters focal adhesion formation and the cytoskeleton. One theory is that filopodia serve as sensory organelles by interacting with nanotextured surfaces and relaying signals via dynamic actin assembly. However, the biological mechanisms behind nanotopography sensing are unclear. The scale of the nanotextured features regulates the specific cell behaviors induced through this process. This nano topography increase can enhance cell adhesion, likely by increasing surface area and binding sites for focal adhesions [75,77,78].

3.2.3. TEM

TEM can visualize the core-shell structure of the fibers. As shown in Fig. 5, TEM images of sample 1E confirm the formation of core-shell morphology in fibers with varying diameters. Fig. 5(A) presents a fiber with a total diameter of 227 nm enclosing a 98.05 nm core. Fig. 5 (B) in addition to the core-shell structure of fibers (highlighted by arrows) also depicts HNT nanoparticles embedded within the core-shell fibers (marked by circle) and distributed along their length. Several studies have shown that the alignment of nanotubes or nanorods like HNT, or alumina nanowires along fiber directions can enhance the mechanical properties and load-bearing capacity of electrospun fibers [32,33].

3.2.4. EDS

EDS is an analytical technique that identifies the elemental composition of materials. To confirm the presence of HNTs in the scaffold structures EDS analysis was applied to detect two elements Si and Al as they are HNT components. EDS can also help to visually assess the uniform distribution of HNTs in the samples. As illustrated in Fig. 6(A),

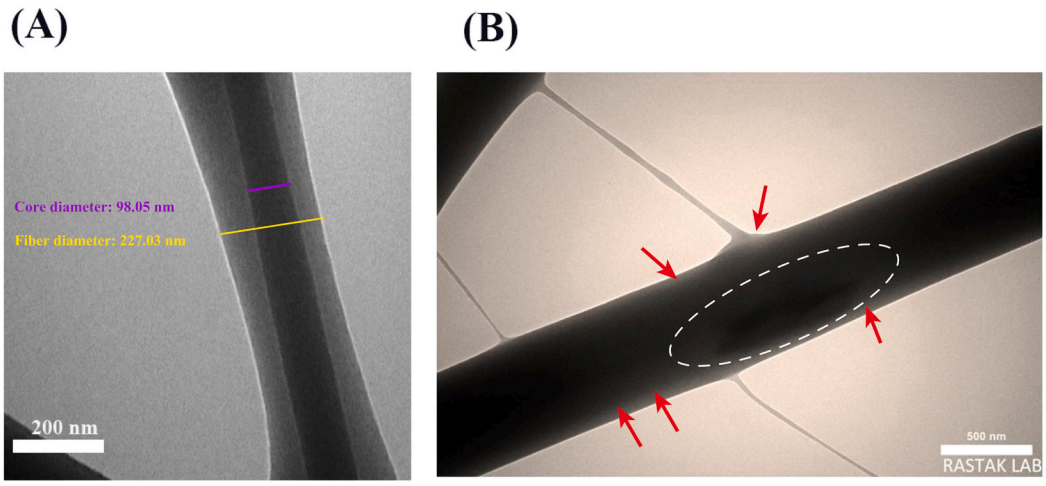

Fig. 5. TEM image of two distinct fibers: (A) 1E core-shell scaffold with 227.03 nm diameter, (B) The presence of nanoparticles in the structure of 1E core-shell fiber (Arrows show the shell layer and the circle mark shows HNT embedded within the fiber).

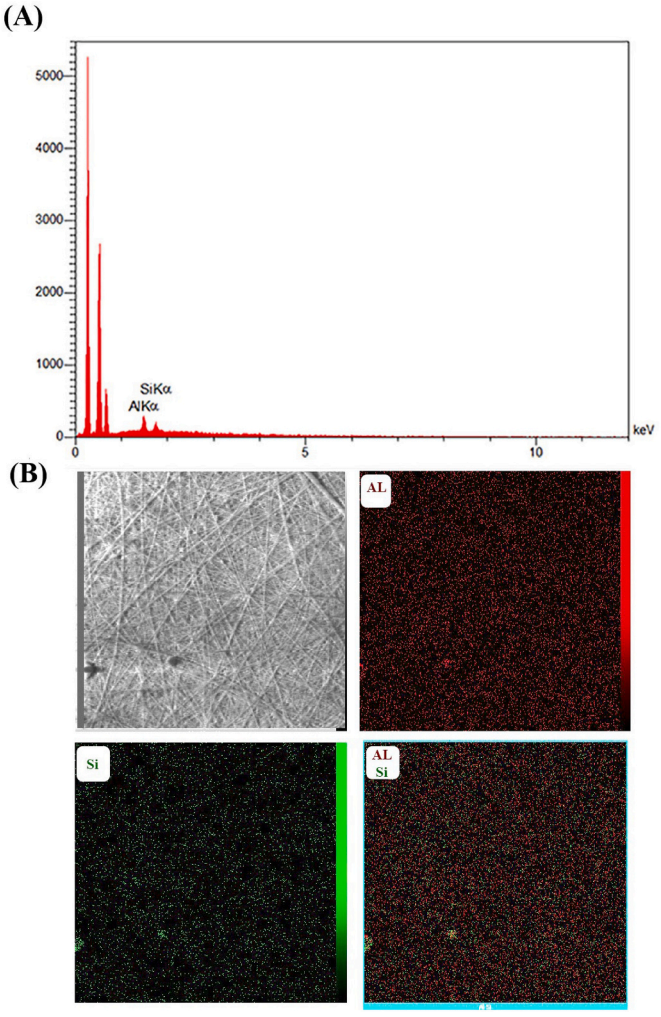

Fig. 6. (A) EDS spectrum representative Al and Si peaks of HNTs in 1E scaffold, (B) EDS elemental maps for Al and Si in HNT structure presented in 1E scaffold.

the EDS spectrum shows characteristic peaks for Al at approximately 1.487 keV (Kα line) and Si at approximately 1.740 keV (Kα line). These peaks indicate the presence of halloysite nanotubes which are composed of aluminosilicates [56,79].

Fig. 6(B) presents the EDS elemental maps for Al and Si (the weight percent and atomic percent of Al and Si of HNTs are represented in Table S1). The maps can evident the almost homogenous dispersion of HNT within the polymeric matrix. The absence of agglomeration or clustering is indicative of uniform distribution [56,57]. It should be noted that the concentration of HNT is a key factor in achieving the uniform dispersion of nanotubes [80]. However, in the previous study, the appropriate amount of HNT (3 wt%) was optimized to avoid agglomeration and gain uniform fibers without beads. In higher amounts of HNTs viscosity increases and agglomeration occurs [33].

3.3. FTIR

FTIR analysis in Fig. 7(A) shows key functional groups in PHB, Cs, and HNT samples. The PHB spectrum displayed characteristic peaks at 1722 cm^{-1} and 1183 cm^{-1} related to C═O stretching band, and C-O-C stretching vibrations. Other PHB peaks were recorded at 981 cm^{-1} for C—C symmetric stretching and 2980 cm^{-1} for aliphatic C—H stretching [57].

For Cs, peaks at 2877 cm^{-1} and around 3353 cm^{-1} were attributed to -CH and -OH stretching vibrations, respectively. Peaks at 1650 cm^{-1} and 1597 cm^{-1} belong to amide I and II bands of the Cs structure [81,82].

The HNT spectrum exhibited bands from 3628 to 3696 cm^{-1} assigned to Al_2OH stretching vibrations. Peaks at 798 cm^{-1} and 749 cm^{-1} were attributed to out-of-plane OH bending and external Si-O-Al vibration. Si—O stretching was indicated by bands at 1115 cm^{-1} and around 1020 cm^{-1}. Bands at 3490 cm^{-1} and 1640 cm^{-1} were ascribed to water molecules and OH groups of water within the HNT tubes [82].

The effects of incorporating HNTs into PHB-Cs blends (core of fibers) were extensively detailed in our previous work [33]. Briefly summarizing, the addition of HNTs was found to introduce hydrogen bonding interactions between the hydroxyl groups on the HNT surface and the carbonyl moieties of PHB along with the amide units of Cs. This was evidenced by shifts in the C═O stretching vibration of PHB at 1722 cm^{-1} and its interaction with the amide I and II bands of Cs (as a shoulder peak) to a broader peak [33,83]. However, here due to the relatively low HNT concentration, the characteristic HNT peak at 3691 cm^{-1} corresponding to Al-OH stretching is not clearly observable in the final blend spectrum. Our prior analyses comprehensively demonstrate that HNTs induce intermolecular hydrogen bonding when incorporated into PHB-Cs matrices but without a dominant spectral signature at the blending ratios used here [33,57].

In Fig. 7(B), the ECM spectrum exhibited peaks at 1665, 1550, 1246, and 3400 cm^{-1} corresponding to amide I, II, III, and amide A groups

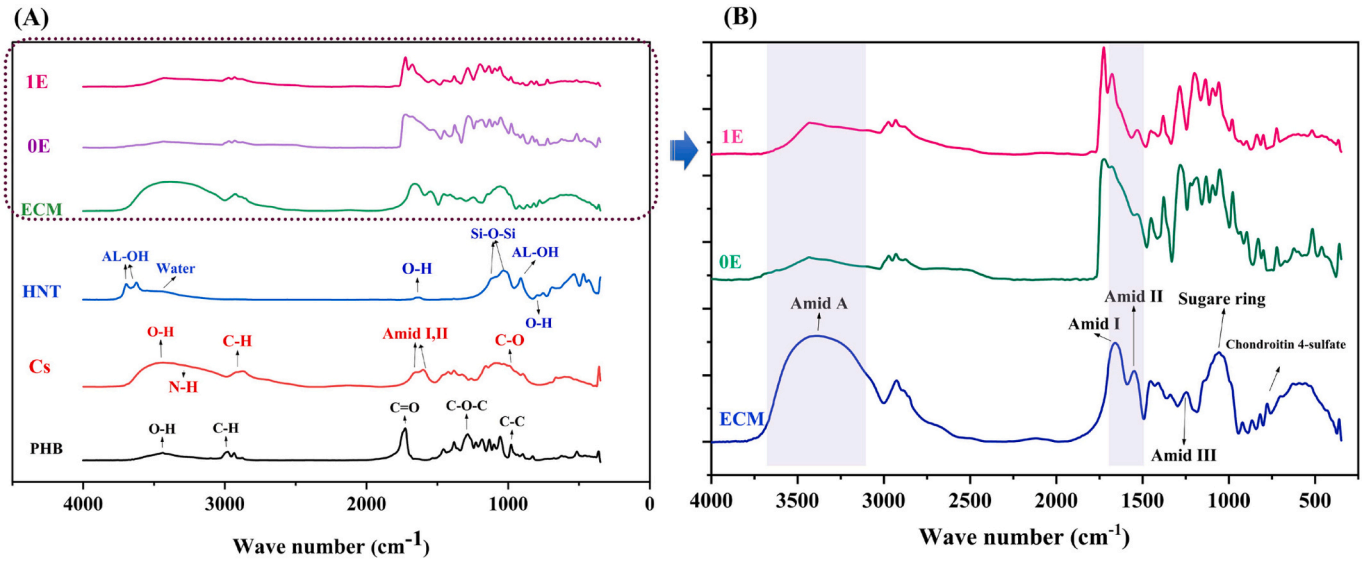

Fig. 7. (A) FTIR spectra of PHB, Cs, HNT, ECM, 0E, and 1E, (B) FTIR spectra magnification of ECM, 0E, and 1E presenting functional group.

respectively [84–86]. As shown in Fig. 7(A), the Cs and ECM spectra overlap significantly due to similar functional group compositions, making them very comparable across much of the range [85]. This similarity results in only minor differences between the FTIR traces of 0E without ECM versus 1E with ECM inclusion. However, a closer image in Fig. 7(B) reveals the presence of ECM in scaffold 1E, which enhanced the intensities of the amide I and II peaks. Also, the amide A peak appears more prominent in 1E compared to 0E. The amide I and II bands present in the ECM spectrum originate from its collagen content [85,87]. In summary, while the FTIR fingerprints of Cs and ECM are very similar, careful analysis verifies successful ECM incorporation into the 1E scaffolds through changes in Amide peaks arising from the collagen component.

3.4. Raman spectroscopy

Fig. 8 illustrates the Raman spectra of ECM, 0E, and 1E scaffolds. The ECM spectrum shows peaks in the 800–1800 cm^{-1} range. These peaks are respectively related to collagen, glycosaminoglycans (GAGs), and water content in the native ECM structure [88].

The 0E scaffold spectrum exhibits a peak at 690–700 cm^{-1} that belongs to N—H bending and pyranose ring vibrations of Cs. This peak, which is marked with a red arrow, is an indicator of Cs presence in scaffolds [89,90]. Similar Cs peaks were observed for the PHB-Cs and PHB-Cs/HNT scaffolds in our previous work [33]. Also, the Raman spectra of the 0E and 1E scaffolds exhibit a prominent peak at 2938 cm^{-1}, which can be assigned to the antisymmetric stretching vibration of the CH_2 group in PHB [33].

In ECM, the collagen-related peak appears at 879 cm^{-1} within the 800–970 cm^{-1} range. For the 1E scaffold, this collagen peak is shifted to lower wavenumbers (670–948 cm^{-1}) with a maximum at 804 cm^{-1}. The collagen peak presence and shift in the optimized 1E scaffold suggests hydrogen bonding between collagen amides and Cs. It should be noted that the Cs peak stemming from NH_2 and pyranoid ring vibrations was overwhelmed in the scaffold spectrum by the prominent collagen peak, appearing as a shoulder rather than as a distinct band [88].

Overall, the Raman spectra provide evidence of ECM components retention (like collagen) in the scaffolds and specific molecular interactions between the ECM components and Cs in the shell of fibers.

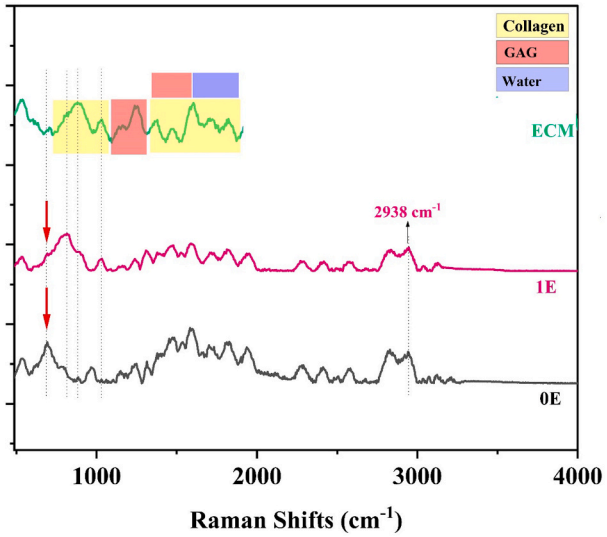

Fig. 8. Raman spectra of ECM, 0E, and 1E scaffolds.

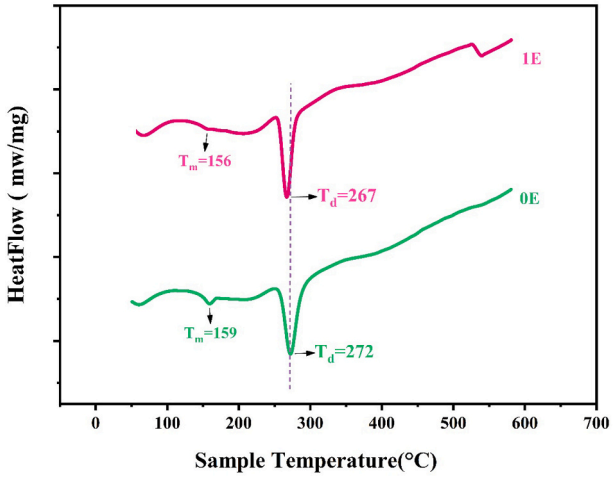

Fig. 9. DSC curves of 0E and 1E scaffolds.

3.5. DSC

The diagrams related to the DSC analysis of scaffolds 1E and 0E are shown in Fig. 9. The addition of ECM lowered the melting temperature (T_m), degradation temperature (T_d), and crystallinity of the scaffold (X_C) as well as the melting enthalpy (ΔH_m), as explained in Table 5. T_m for the scaffold without ECM was 159 °C, which decreased to 156 °C after adding ECM. Also, the T_d dropped from 272 °C to 267 °C. The lowered T_m and T_d are likely due to the ECM molecules separating the Cs chains slightly, reducing intermolecular interactions. As expected, the presence of ECM in the structure reduced the crystallinity from 18 % for the 0E scaffold to 11.3 % for the 1E scaffold. The decreased crystallinity is likely because the ECM made interactions with Cs and changed the semi-crystalline structure of Cs [91]. The added ECM resulted in more amorphous regions and fewer crystalline areas in the scaffold.

In a study by Feng et al. [92], adding ECM to PCL, reduced the crystallinity of electrospun scaffolds. Authors attributed this reduction in crystallinity to the increased mobility of polymer chains after the addition of ECM to the structure. In another study, Chen et al. [93] investigated the intermolecular interactions in electrospun collagen–Cs nanofibers. They reported that the enthalpy for the Cs-collagen blend is lower than the enthalpy for each of these single components. The authors concluded that hydrogen bonds formed between these two different macromolecules compete with the hydrogen bonding between molecules of the same polymer, replacing them and affecting enthalpy and crystallinity.

3.6. Analysis of surface hydrophilicity

Fig. 10(A) shows the water contact angle of the scaffolds. Adding ECM to the scaffold structure increased the contact angle from 42° (for scaffold 0E) to 85° (for scaffold 5E), as depicted in Fig. 10(B). Although some studies have mentioned increased hydrophilicity by adding ECM, many reports show that ECM addition decreases the hydrophilicity. In a study by Xu et al. [94], Cs-gelatin scaffolds were examined with decellularized ECM. The results showed ECM significantly increased the surface contact angle. In that study, the contact angle was 144.3° for pure ECM and 84.84° for the Cs-gelatin scaffold. Adding 2 wt% ECM to the scaffold increased the contact angle from 84.84° to 114.25°. Another study by Bual et al. [95] made scaffolds from PCL, gelatin, and ECM. Their results showed scaffolds with 10 % gelatin had a 64.8° contact angle. Adding 5 wt% ECM increased it to 78.8°. Scaffolds with 5 % PCL and 10 % gelatin had a contact angle below 10°, which increased to 38.5° after adding 5 % ECM.

Indeed, several factors impact contact angle, including hydrogen bonds between Cs and ECM, surface roughness, and surface charge density [96]. Also, the ECM amphiphilic molecules like proteoglycans and glycosaminoglycans (GAGs) have hydrophilic and hydrophobic regions. Cs is a natural polysaccharide consisting of positively charged amino groups [91]. When ECM is added to the Cs solution, hydrogen bonds can form (as supported by FTIR and Raman analysis), involving hydrophilic groups. Also, chitosan's positively charged amines can interact electrostatically with the negatively charged sulfate or carboxyl groups of GAGs. The binding of the ECM's hydrophilic parts to Cs means the hydrophobic parts are not involved in the interaction, remain free, and are exposed to water molecules. This can decrease the Cs-ECM complex's overall hydrophilicity. In other words, ECM's amphiphilic parts interact with Cs and reduce the availability of hydrophilic areas to interact with water, and hydrophilicity decreases [97].

In this study, although adding ECM increased the contact angle, the scaffolds are still hydrophilic. Many studies note the ideal contact angle for cell adhesion is 60–70° [98,99]. Thus, the 1E scaffold likely shows a higher potential for cell adhesion compared to the 0E scaffold.

Table 5
Melting temperature (T_m), degradation temperature (T_d), crystallinity (X_C) and melting enthalpy (ΔH_m) of 0E and 1E scaffolds obtained from DSC analysis.

Samples	T_m (°C)	T_d (°C)	ΔH_m	X_c %
0E	159	272	15.55	18
1E	156	267	9.8	11.3

3.7. Mechanical characterization

As noted in some literature, articular cartilage is exposed to constant static tension due to the presence of negatively charged proteoglycans within its ECM. These proteoglycans retain fluid and cause the collagen in the cartilage matrix to experience tension. This tension is necessary for swelling without rupture. To mimic the tensile properties of articular cartilage, the ultimate tensile strength of the scaffold should be between 2 and 8 MPa [100,101].

Fig. 11 represents scaffolds' stress-strain curves; in Fig. 12(A), their ultimate strength is compared. The results indicate that adding 1 wt% ECM significantly improved the scaffold's mechanical strength ($p < 0.05$), whereas 3 wt% and 5 wt% ECM had no significant effect on the final strength of the scaffolds. The final strength of 1E scaffold was 5.81 MPa which meets the desired range of articular cartilage. Adding 3 wt% and 5 wt% ECM did not change the final strength of scaffolds significantly. However, the scaffold's mechanical properties decreased at higher ECM concentrations (3 wt% and 5 wt%). This phenomenon at higher amounts of ECM may be due to ECM molecules agglomeration, which could interfere with interactions between the scaffold materials and ECM. Also, at higher ECM concentrations, crystallinity decreases substantially. The combination of these factors can decrease mechanical properties [48].The improved mechanical properties of the scaffold with 1 wt% ECM can be due to hydrogen bond formation between Cs and ECM. Both Cs and ECM contain functional groups that can form hydrogen bonds, which enhance mechanical properties [102]. Some studies express that Cs-collagen can form ionic bonds and polyanionic-polycationic complexes as well. This complex forms because of the cationic nature of Cs and anionic COOH groups in collagen. These ionic interactions can enhance mechanical properties up to certain ECM concentrations [93].

On the other hand, as stated in Section 3.2.1, adding 1 wt% ECM decreased fiber diameter and made the distribution more uniform. This in turn affects the mechanical properties. Thinner, more uniform fibers mean more fibers participate in bearing stress, improving mechanical properties [33]. In a study by Feng et al. [92], the final properties of PCL-ECM electrospun scaffolds were investigated. The results showed scaffold strength increased from 2.15 ± 0.16 MPa to 3.38 ± 0.6 MPa with ECM incorporation. These specific results were attributed to hydrogen bonds between PCL and ECM.

As stated, in articular cartilage, collagen II fibers are stretched to counteract repulsive forces that arise from negatively charged proteoglycans. Indeed, collagen II fibrils are stretched to prevent tissue ultra-expansion. Considering this mechanism, it is necessary to predict strain capability for cartilage scaffolds as well [101]. Some studies report the strain measured in meniscal cartilage under physiological loading varies in the range of 3–8 % [103]. Fig. 12(B) illustrates the strain of the scaffolds. The strain in 1E scaffold is 3.17 % and is significantly higher than 0E ($p < 0.05$). As the ECM content increased, strain decreased, which can be related to the 3E and 5E group structure. In these groups, the fiber structure becomes so amorphous that prevents the polymeric chains from aligning and stretching more under applied tension.

According to the results of fiber diameter, hydrophilicity, and mechanical analyses, the 1E scaffold was selected as optimal. Further analyses were performed on the 0E and 1E scaffolds.

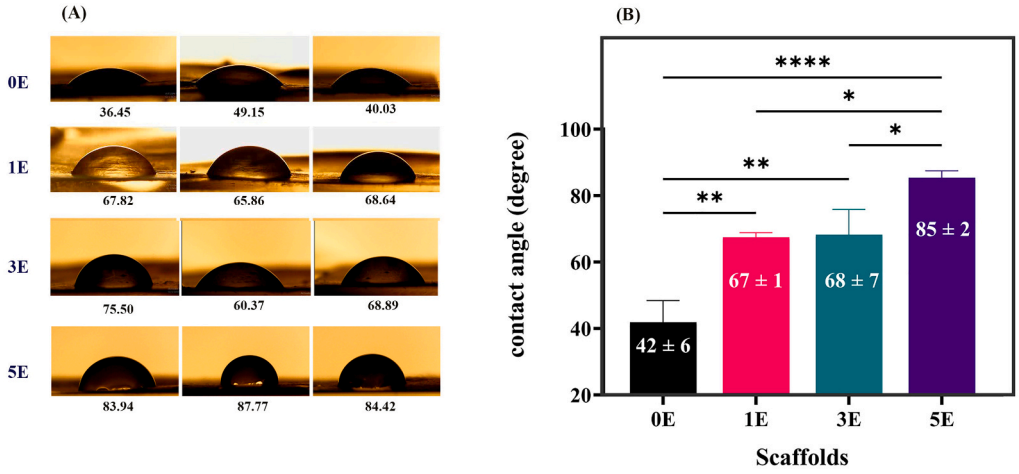

Fig. 10. (A) Image of water drops on the surface of scaffolds, (B) Average of water contact angle on the surface of scaffolds (* $p < 0.05$).

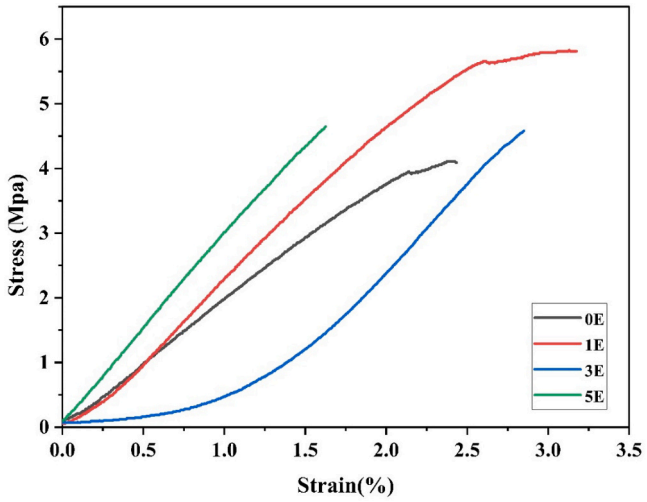

Fig. 11. Stress-strain curves of the scaffolds.

3.8. *In vitro degradation*

3.8.1. *Weight loss evaluation*

Fig. 13(A) shows the weight changes of samples 0E and 1E during the degradation test process. After 100 days, the remaining weight was 59 % for 0E and 52 % for 1E. These findings represent that the 1E scaffold underwent faster weight loss than the 0E scaffold. The faster degradation process can be attributed to the presence of ECMs. In fact, ECM decreases crystallinity, allowing water molecules to penetrate the scaffold bulk faster, and subsequently, hydrolysis accelerates. Despite the reduced crystallinity, other issues can also affect the degradation profile. The weak acid molecules produced during degradation can break more ester bonds and cause faster degradation. The smaller fiber diameter and interconnected pores also facilitate faster degradation [104].

Previous studies indicated that the formation of cartilage ECM can take at least 8 weeks. Despite a weight loss of approximately 40 %, the 1E scaffold retained 60 % of its initial weight within eight weeks. It suggests that its ability to support tissue regeneration is comparable to the natural rate of cartilage tissue growth [59,105].

3.8.2. *pH changes*

Measuring the pH changes during the degradation process is important in order to check whether the degradation products cause extreme and uncontrolled pH changes in the surrounding microenvironment. Fig. 13(B) shows the pH change trends. Scaffold 1E displayed a faster decreasing pH trend. After 100 days, the pH was 6.84 for the scaffold without ECM and 6.69 for the scaffold with ECM. The presence of ECM in the 1E scaffold structure and the release of its degradation products can be considered as a key factor that causes the pH change. It should be noted that at any time point, more amount (by weight) of the 1E scaffold material had degraded compared to the 0E scaffold. It means that more degradation products are released into the solution. Regardless of the ECM presence, this difference alone can cause remarkable pH changes in the 1E solution compared to the 0E solution [62].

Interestingly, degradation products of ECM-containing scaffolds *in vivo* can affect cell behavior, and influence chemotaxis and mitogenesis. A study by Reing et al. [106] on porcine bladder ECM scaffolds revealed

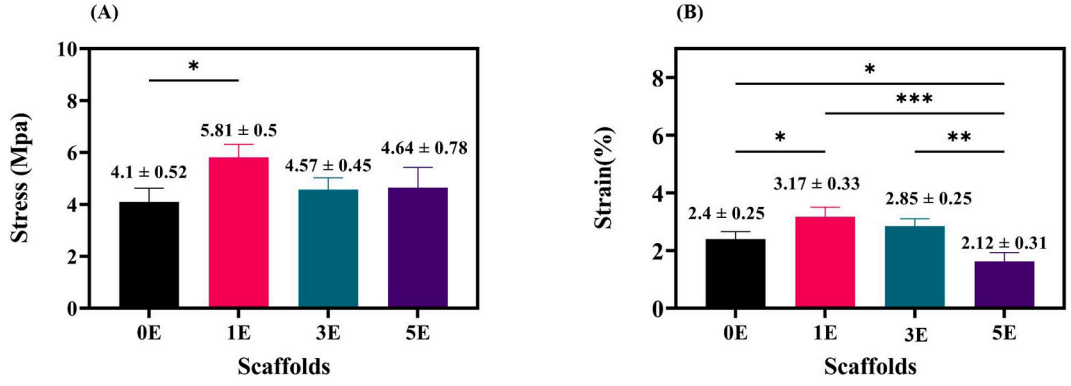

Fig. 12. (A) Tensile strength and (B) elongation at break of scaffolds (*$p < 0.05$, **$p < 0.01$, *** $p < 0.001$).

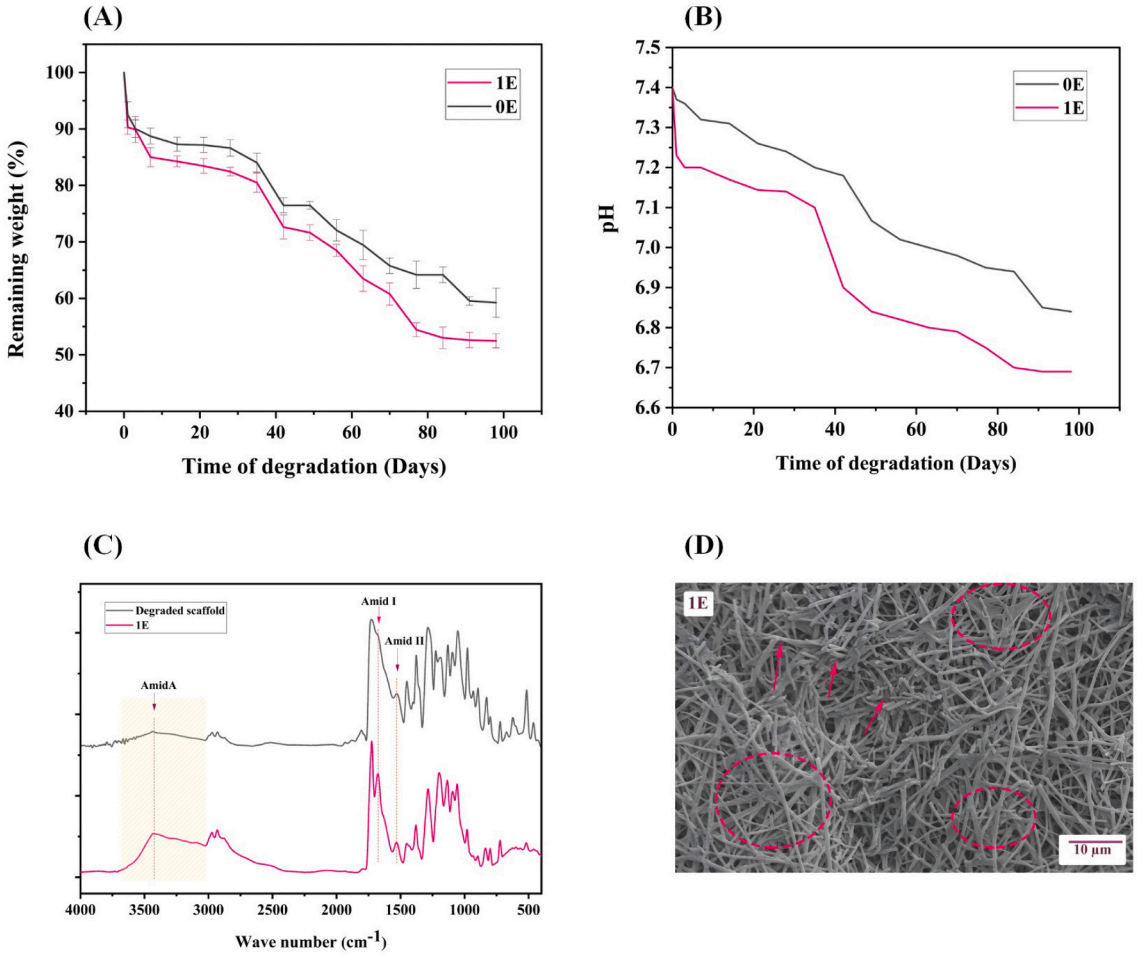

Fig. 13. (A) Weight change, (B) pH change of 0E and 1E scaffolds during 100 days of degradation, (C) FTIR of 1E scaffold before and after 100 days of degradation, and (D) SEM image of 1E scaffold after 100 days of degradation (Circles indicate surface melting and arrows represent fiber breakage).

that ECM scaffold degradation products attract and stimulate proliferation in progenitor (undifferentiated) cells while inhibiting migration and proliferation in mature endothelial cells. This selective influence is likely due to growth factors in the ECM. Understanding these interactions can help to select specific cell types to improve tissue repair and regeneration.

3.8.3. FTIR assessment

Fig. 13(C) shows the FTIR spectrum of scaffold 1E on the final day of the degradation test. As seen in the image, the peaks related to amide I, amide II, and amide A in the FTIR spectrum are weakened after degradation. This phenomenon can be attributed to the destruction of amide bonds in the ECM collagen and Cs structure [62].

In a study by Mancipe et al. [62], core-shell scaffolds were produced for wound healing with PCL in the core and PVA-collagen shell. Similarly, the degradation test showed decreased intensity and area under the peaks related to amide I, II, and III after degradation, attributed to collagen structure destruction.

3.8.4. Morphology of the fibers

Fig. 13(D) shows the morphology of the 1E fibers after the 100-day degradation process. As can be seen in the picture, in the major parts of the scaffold, surface melting (marked with circles) and fiber breakage (highlighted with arrows) have occurred. The degradation behavior of electrospun fibers in PBS is affected by molecular weight reduction and the structural characteristics of crystalline and amorphous regions during degradation [107]. Hydrolytic degradation at first affects the amorphous regions of PHB and Cs, leading to a decrease in molecular weight. As the polymer chains shorten, the glass transition temperature (T_g) of the amorphous phase decreases. When T_g decreases below environmental temperature, chain mobility in these regions increases [59]. This phenomenon reduces surface tension and causes fibers to adhere and fuse. The subsidence of the scaffold layers and the unification of fibers (sticking of fibers to each other) also occurred due to the presence of a high percentage of Cs in the structure as well as ECM, which led to an increase in the amorphous nature of the core-shell scaffolds. In contrast, the crystalline domains of PHB remain rigid, as hydrolysis progresses in the amorphous phase. Since polymer chains in crystalline regions have less mobility, they cannot relax or rearrange, leading to brittle fractures in some regions [32].

3.9. Cellular assay

3.9.1. Cell attachment

Fig. 14 visualizes the cellular morphology and distribution on the surfaces of 0E and 1E scaffolds at days 1 and 7 after seeding. SEM graphs revealed that a greater area of scaffold 1E was covered by chondrocytes and secreted more ECM on day 7 than scaffold 0E. This issue is likely originated from several factors, including hydrophilicity, fiber diameter, surface roughness, and ECM content of 1E scaffold, as explained in previous analyses [33,44,57]. The appropriate amphiphilicity of scaffold 1E with the incorporation of ECM proteins and macromolecules, can mimic the native microenvironment for the cells. This optimized milieu offers improved cell adhesion and proliferation on the scaffold surface

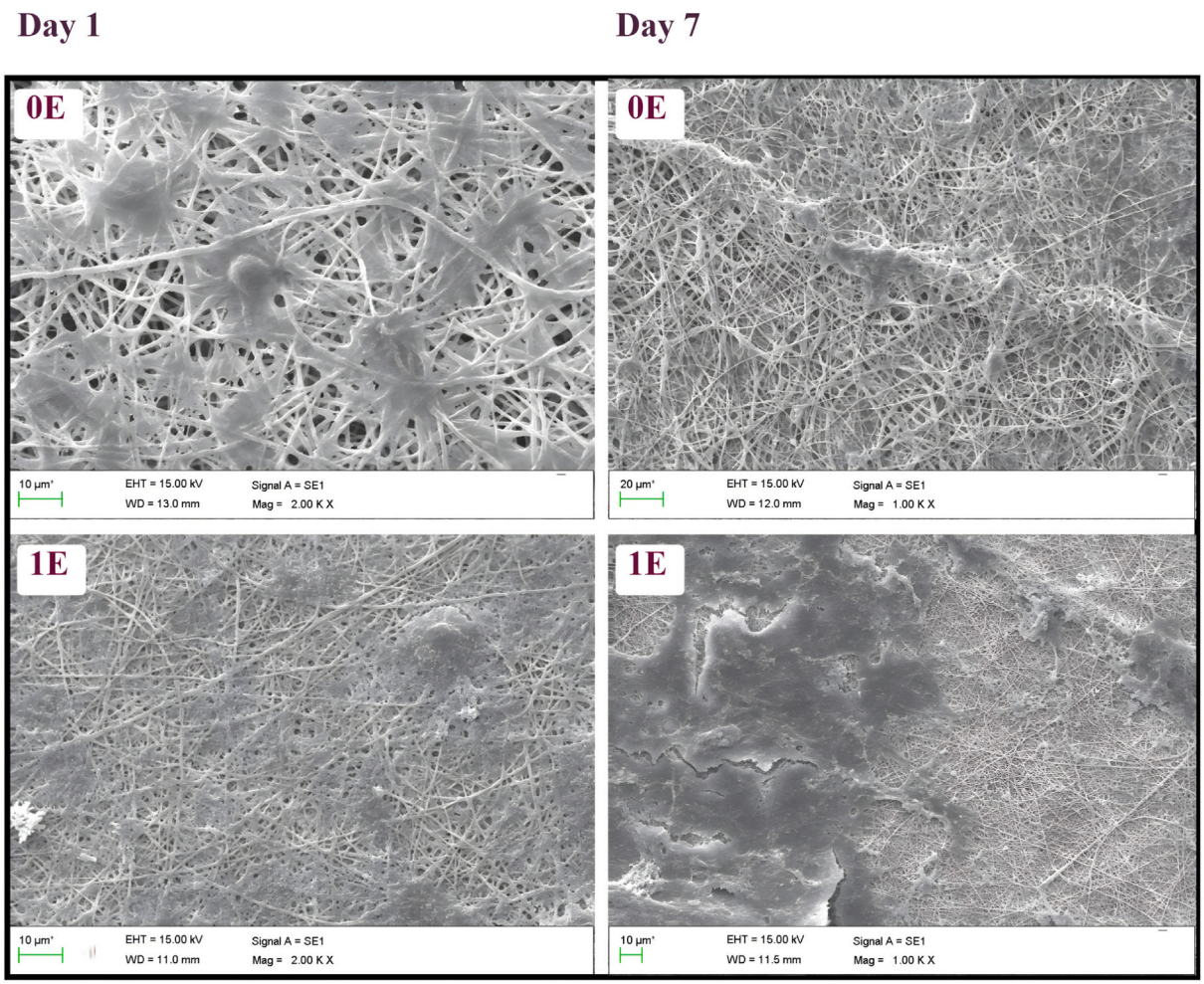

Fig. 14. SEM images of 0E and 1E scaffolds after 1 day (2000×) and 7 days (1000×) of chondrocyte culture.

[59].

Previous studies have verified that chondrocytes can secret more ECM on surfaces made of thinner fibers as observed here in the 1E scaffold [44,108]. Moreover, according to AFM analysis surface roughness of scaffold 1E was more than 0E. This characteristic can also enhance cell adhesion and provide more anchorage site [109].

3.9.2. Cell viability

Fig. 15 presents the cell viability of 0E and 1E scaffolds on days 1, 3, and 7 as a result of the MTT assay. Cell viability for both scaffolds (0E and 1E) exceeded 80 % in all days. Moreover, a significant upward trend in cell viability was observed for the 1E scaffold over the seven days ($p < 0.05$). Still, there was no significant difference between the cell viability of the 0E scaffold on different days. These findings indicate that the incorporation of 1 wt% ECM had no detrimental effects on cell viability and proliferation and provided a favorable microenvironment for cellular growth and expansion. Furthermore, while there were no significant differences in cell viability between the two scaffolds, it is hypothesized that the presence of ECM may have influenced gene expression and chondrogenic differentiation. This suggests that cells cultured on the 1E scaffold might spend some of their energy on these processes rather than prioritizing cell proliferation [110].

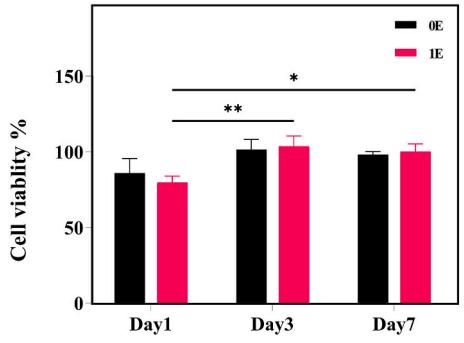

Fig. 15. Cell viability of chondrocyte after 1, 3, and 7 days of culture on 0E and 1E scaffolds (*$p < 0.05$ and **$p < 0.01$).

In a study by T. Xiao et al. [111], the cell viability and chondrogenesis of two scaffolds fabricated from articular cartilage ECM and Wharton's jelly ECM were compared. The authors reported that although cell proliferation increased on both ECM scaffolds, there was no significant difference between the ECM scaffolds and the control group (absence of ECM). This finding indicates scaffolds' good cell affinity and ability to mimic the native cartilage ECM microenvironment. Meanwhile, the ECM scaffolds upregulated cartilage-specific genes and stimulated chondrogenesis. These results can further verify the present study findings.

3.9.3. DAPI staining

DAPI is a fluorescent dye commonly employed to visualize cell nuclei due to its specific affinity for AT-rich regions of DNA. Upon excitation with ultraviolet light, DAPI emits blue fluorescence, enabling the identification of DNA-containing organelles such as nuclei and mitochondria

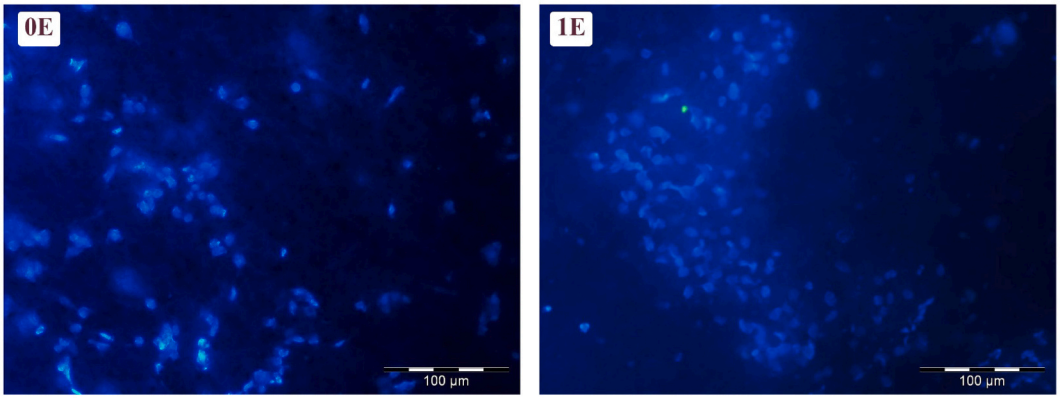

Fig. 16. DAPI staining of chondrocyte after 7 days of culture on 0E and 1E scaffolds.

[112]. Fig. 16 presents fluorescent images of 0E and 1E scaffolds stained with DAPI on the 7th day of cell culture. Remarkably, the 1E scaffold demonstrated a higher density of stained cell nuclei and covered a larger area of the surface with cells than the 0E scaffold. These findings strongly suggest its enhanced ability to promote cell survival and growth, likely attributed to the scaffold's ECM composition. These findings align with the results obtained from the MTT and cell attachment assay.

3.9.4. Gene expression analysis

To investigate the influence of the ECM on chondrogenesis and chondrocyte phenotype, the expression of chondrocyte-specific genes was examined using reverse transcription-quantitative polymerase chain reaction (RT-qPCR) over 21 days. The transcriptional levels of *COL II*, *AGC*, and *SOX 9*, key markers of the chondrocyte phenotype, were assessed. Also, the expression of *COL X*, as a marker of chondrocyte hypertrophy, was analyzed [60,113].

COL II expression is a feature of mature chondrocytes and indicates chondrogenic differentiation [44]. As depicted in Fig. 17(A), *COL II* expression is higher in the 1E scaffold compared to the 0E scaffold across all time points ($p < 0.05$). Comparison of *COL II* expression between the two scaffolds will explain the influence of the ECM on chondrocyte differentiation and matrix synthesis. Additionally, *AGC* expression was significantly increased in the 1E scaffold compared to the 0E scaffold at

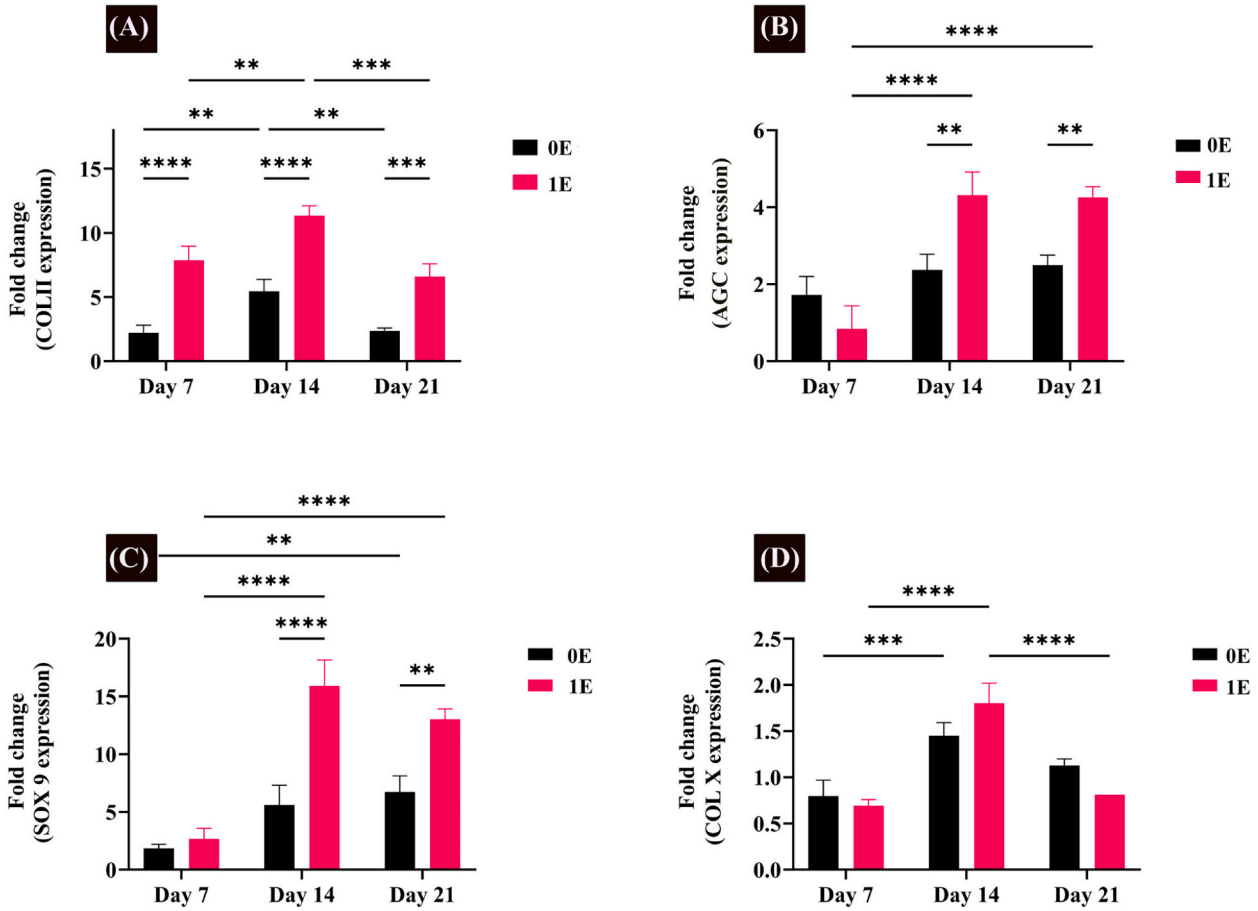

Fig. 17. (A) *COL II*, (B) *AGC*, (C) *SOX 9*, and D) *COL X* expression of chondrocytes after 7,14, and 21 days of culture on 0E and 1E scaffolds (*$p < 0.05$, **$p < 0.01$, ***$p < 0.001$, and ****$p < 0.0001$).

days 14 and 21 of culture ($p < 0.05$), as shown in Fig. 17(B).

SOX 9 is a main regulator of chondrogenesis and orchestrates multiple stages of cartilage development. This transcription factor binds to DNA sequences and activates genes essential for cartilage formation, including *COL II* and AGC. Several genetic studies in humans and mice confirm its critical role in chondrogenesis [114]. Fig. 17(C) shows *SOX 9* expression is significantly higher in the 1E scaffold group compared to the 0E group after 14 and 21 days of cell culture ($p < 0.05$). It represents that ECM content contributes to the upregulation of *SOX 9*, a key regulator of chondrogenesis.

COL X is a specific collagen type that is over-expressed during hypertrophic chondrocyte differentiation. Its upregulation indicates chondrocyte transition from proliferative to hypertrophic phase. As chondrocytes mature and prepare for endochondral ossification, *COL X* expression increases significantly [115]. According to Fig. 17(D), *COL X* expression within the 1E scaffold has increased from day 7 to 14, and after that decreased from day 14 to 21. On day 21, the expression of *COL X* in group 1E was lower than in group 0E. Although this difference is not significant. Also, there is no significant difference in *COL X* expression between 0E and 1E groups at different time points. These findings indicate that ECM incorporation in the 1E scaffold did not stimulate *COL X* expression.

in a study by Lu et al. [60], the effect of cartilage ECM incorporation into collagen scaffold on the chondrogenesis of BMSC was investigated. The ECM was added to the collagen matrix in the form of particles and solubilized. They reported that *SOX 9*, *AGC*, and *COL II* expression were upregulated over 21 days. Solubilized ECM even represented better results than particle ECM. Consistent with our findings, the *COL X* expression increased from day 7 to 14 but was suppressed to day 21. Similar to the present study, *COL X* expression was lower in the ECM-containing scaffold, however, there was no significant difference in all groups. These results again confirm that ECM facilitates chondrogenesis while at least not promoting hypertrophy.

In another study by Li et al. [115], the effect of cartilage ECM scaffolds on chondrocyte hypertrophy was investigated. For this, collagen I and ECM scaffolds were fabricated through the freeze-drying method. The results of the study showed transcription levels of *COL II*, *AGC*, and *SOX 9* were significantly higher in chondrocytes cultured on ECM scaffolds than cells cultured on collagen I scaffold. Furthermore, genes related to chondrocyte hypertrophy, including *COL X*, were significantly downregulated in chondrocytes cultured in the ECM scaffold. In conclusion, the ECM scaffold supported the phenotype preservation of chondrocytes.

4. Conclusion

This study aimed to design and characterize core-shell electrospun scaffolds, incorporating cartilage ECM. SEM images showed that the incorporation of ECM within the shell decreased fiber diameter and increased fiber uniformity. FTIR and Raman analyses revealed interactions between Cs and ECM, resulting from hydrogen bond formation. According to DSC analysis crystallinity and melting temperature of ECM-incorporated core-shell scaffolds decreased. While ECM presence moderated scaffold hydrophilicity, it significantly augmented mechanical properties (tensile strength and strain) at the 1 wt% ECM concentration. However, scaffold biodegradability was also accelerated due to increased amorphicity. The core-shell scaffold containing 1 wt% ECM displayed superior cellular viability, proliferation, and chondrogenic capacity compared to other groups. This scaffold also showed upregulated cartilage-specific gene expressions. These findings suggest that the electrospun core-shell scaffold with 1 wt% ECM (1E scaffold) could serve as a valuable platform for the next step of investigations, such as *in vivo* studies, advanced cellular analysis, and micro-CT imaging, in the context of cartilage tissue engineering.

CRediT authorship contribution statement

Sepideh Ghadirian: Writing – original draft, Visualization, Validation, Resources, Methodology, Investigation, Formal analysis, Conceptualization. **Laleh Shariati:** Writing – review & editing, Validation. **Saeed Karbasi:** Writing – review & editing, Validation, Supervision, Resources, Funding acquisition, Conceptualization.

Declaration of competing interest

The authors declare that they have no known competing financial interests or personal relationships that could have appeared to influence the work reported in this paper.

Acknowledgment

This project has received funding from Isfahan University of Medical Sciences under grant number 3991011.

Appendix A. Supplementary data

Supplementary data to this article can be found online at https://doi.org/10.1016/j.bioadv.2025.214249.

Data availability

Data will be made available on request.

References

[1] A. Zelinka, A.J. Roelofs, R.A. Kandel, C. De Bari, Cellular therapy and tissue engineering for cartilage repair, Osteoarthr. Cartil. 30 (2022) 1547–1560, https://doi.org/10.1016/j.joca.2022.07.012.
[2] T. Li, B. Liu, K. Chen, Y. Lou, Y. Jiang, D. Zhang, Small molecule compounds promote the proliferation of chondrocytes and chondrogenic differentiation of stem cells in cartilage tissue engineering, Biomed. Pharmacother. 131 (2020) 110652, https://doi.org/10.1016/j.biopha.2020.110652.
[3] Y. Wang, M. Du, T. Wu, T. Su, L. Ai, D. Jiang, The application of ECM-derived biomaterials in cartilage tissue engineering, Mechanobiol. Med. 1 (2023) 100007, https://doi.org/10.1016/j.mbm.2023.100007.
[4] Z. Zhang, Y. Mu, H. Zhou, H. Yao, D.-A. Wang, Cartilage tissue engineering in practice: preclinical trials, clinical applications, and prospects, Tissue Eng. Part B Rev. 29 (2023) 473–490, https://doi.org/10.1089/ten.teb.2022.0190.
[5] Y. Li, M. Zhou, W. Zheng, J. Yang, N. Jiang, Scaffold-based tissue engineering strategies for soft–hard interface regeneration, Regen. Biomater. 10 (2023) rbac091, https://doi.org/10.1093/rb/rbac091.
[6] A. Keirouz, Z. Wang, V.S. Reddy, Z.K. Nagy, P. Vass, M. Buzgo, S. Ramakrishna, N. Radacsi, The history of electrospinning: past, present, and future developments, Adv. Mater. Technol. 8 (2023) 2201723, https://doi.org/10.1002/admt.202201723.
[7] M. Mohammadalipour, T. Behzad, S. Karbasi, Z. Mohammadalipour, Theoretical and experimental investigation of solubility and Young's modulus models for polyhydroxybutyrate-based electrospun scaffolds, J. Appl. Polym. Sci. 140 (2023) e53666, https://doi.org/10.1002/app.53666.
[8] M. Mohammadalipour, T. Behzad, S. Karbasi, Z. Mohammadalipour, Optimization and characterization of polyhydroxybutyrate/lignin electro-spun scaffolds for tissue engineering applications, Int. J. Biol. Macromol. 218 (2022) 317–334, https://doi.org/10.1016/j.ijbiomac.2022.07.139.
[9] Y. Liu, L. Liu, Z. Wang, G. Zheng, Q. Chen, E. Luo, Application of electrospinning strategy on cartilage tissue engineering, Curr. Stem Cell Res. Ther. 13 (2018) 526–532.
[10] M. Rahmati, D.K. Mills, A.M. Urbanska, M.R. Saeb, J.R. Venugopal, S. Ramakrishna, M. Mozafari, Electrospinning for tissue engineering applications, Prog. Mater. Sci. 117 (2021), https://doi.org/10.1016/j.pmatsci.2020.100721.
[11] A.H. Tehrani, A. Zadhoush, S. Karbasi, S.N. Khorasani, Experimental investigation of the governing parameters in the electrospinning of poly(3-hydroxybutyrate) scaffolds: structural characteristics of the pores, J. Appl. Polym. Sci. 118 (2010) 2682–2689, https://doi.org/10.1002/app.32620.
[12] J. Khan, A. Khan, M.Q. Khan, H. Khan, Applications of co-axial electrospinning in the biomedical field, Next Mater. 3 (2024) 100138, https://doi.org/10.1016/j.nxmate.2024.100138.
[13] T. Jiang, E.J. Carbone, K.W.H. Lo, C.T. Laurencin, Electrospinning of polymer nanofibers for tissue regeneration, Prog. Polym. Sci. 46 (2015) 1–24, https://doi.org/10.1016/j.progpolymsci.2014.12.001.
[14] L.E. Sperling, K.P. Reis, P. Pranke, J.H. Wendorff, Advantages and challenges offered by biofunctional core–shell fiber systems for tissue engineering and drug delivery, Drug Discov. Today 21 (2016) 1243–1256.

[15] J. Baek, E. Lee, M.K. Lotz, D.D. D'Lima, Bioactive proteins delivery through core-shell nanofibers for meniscal tissue regeneration, nanomedicine nanotechnology, Biol. Med. 23 (2020) 102090, https://doi.org/10.1016/j.nano.2019.102090.
[16] Y. Zheng, B. Xue, B. Wei, B. Xia, S. Li, X. Gao, Y. Hao, Y. Wei, L. Guo, H. Wu, Y. Yang, X. Gao, B. Yu, Y. Zhang, S. Yang, Z. Luo, T. Ma, J. Huang, Core-shell oxygen-releasing fibers for annulus fibrosus repair in the intervertebral disc of rats, Mater. Today Bio. 18 (2023) 100535, https://doi.org/10.1016/j.mtbio.2022.100535.
[17] A.S. Pryadko, V.V. Botvin, Y.R. Mukhortova, I. Pariy, D.V. Wagner, P. P. Laktionov, V.S. Chernonosova, B.P. Chelobanov, R.V. Chernozem, M. A. Surmeneva, A.L. Kholkin, R.A. Surmenev, Core-shell magnetoactive PHB/gelatin/magnetite composite electrospun scaffolds for biomedical applications, Polymers (Basel) 14 (2022), https://doi.org/10.3390/polym14030529.
[18] M. Yousefzadeh, F. Ghasemkhah, Design of Porous, Core-Shell, and Hollow Nanofibers, Handb. Nanofibers, Springer, in, 2019, pp. 157–214.
[19] N. Kazemi, M. Javad Mahalati, Y. Kaviani, M.H. Al-Musawi, J. Varshosaz, S. Soleymani Eil Bakhtiari, M. Tavakoli, M. Alizadeh, F. Sharifianjazi, S. Salehi, A. Najafinezhad, M. Mirhaj, Core-shell nanofibers containing L-arginine stimulates angiogenesis and full thickness dermal wound repair, Int. J. Pharm. 653 (2024) 123931, https://doi.org/10.1016/j.ijpharm.2024.123931.
[20] J.C. Silva, R.N. Udangawa, J. Chen, C.D. Mancinelli, F.F.F. Garrudo, P.E. Mikael, J.M.S. Cabral, F.C. Ferreira, R.J. Linhardt, Kartogenin-loaded coaxial PGS/PCL aligned nanofibers for cartilage tissue engineering, Mater. Sci. Eng. C 107 (2020) 110291, https://doi.org/10.1016/j.msec.2019.110291.
[21] J. Baek, M.K. Lotz, D.D. D'Lima, Core–Shell Nanofibrous Scaffolds for Repair of Meniscus Tears, Tissue Eng. Part A 25 (2019) 1577–1590. doi:https://doi.org/10.1089/ten.tea.2018.0319.
[22] H. Yin, J. Wang, Z. Gu, W. Feng, M. Gao, Y. Wu, H. Zheng, X. He, X. Mo, Evaluation of the potential of kartogenin encapsulated poly(L-lactic acid-co-caprolactone)/collagen nanofibers for tracheal cartilage regeneration, J. Biomater. Appl. 32 (2017) 331–341, https://doi.org/10.1177/0885328217717077.
[23] Z. Mohammadalizadeh, E. Bahremandi-Toloue, S. Karbasi, Synthetic-based blended electrospun scaffolds in tissue engineering applications, J. Mater. Sci. 57 (2022) 4020–4079, https://doi.org/10.1007/s10853-021-06826-w.
[24] M. Esmaeili, S. Ghasemi, L. Shariati, S. Karbasi, Evaluating the osteogenic properties of polyhydroxybutyrate-zein/multiwalled carbon nanotubes (MWCNTs) electrospun composite scaffold for bone tissue engineering applications, Int. J. Biol. Macromol. 276 (2024) 133829, https://doi.org/10.1016/j.ijbiomac.2024.133829.
[25] D. Sadeghi, S. Karbasi, S. Razavi, S. Mohammadi, M.A. Shokrgozar, S. Bonakdar, Electrospun poly(hydroxybutyrate)/chitosan blend fibrous scaffolds for cartilage tissue engineering, J. Appl. Polym. Sci. 133 (2016) 1–9, https://doi.org/10.1002/app.44171.
[26] P. Naderi, M. Zarei, S. Karbasi, H. Salehi, Evaluation of the effects of keratin on physical, mechanical and biological properties of poly (3-hydroxybutyrate) electrospun scaffold: potential application in bone tissue engineering, Eur. Polym. J. 124 (2020) 109502, https://doi.org/10.1016/j.eurpolymj.2020.109502.
[27] M.A. Asl, S. Karbasi, S. Beigi-Boroujeni, S. Zamanlui Benisi, M. Saeed, Evaluation of the effects of starch on polyhydroxybutyrate electrospun scaffolds for bone tissue engineering applications, Int. J. Biol. Macromol. 191 (2021) 500–513, https://doi.org/10.1016/j.ijbiomac.2021.09.078.
[28] S. Saravanan, R.S. Leena, N. Selvamurugan, Chitosan based biocomposite scaffolds for bone tissue engineering, Int. J. Biol. Macromol. 93 (2016) 1354–1365, https://doi.org/10.1016/j.ijbiomac.2016.01.112.
[29] F. Croisier, C. Jérôme, Chitosan-based biomaterials for tissue engineering, Eur. Polym. J. 49 (2013) 780–792, https://doi.org/10.1016/j.eurpolymj.2012.12.009.
[30] M. Tavakoli, S. Karbasi, S., Soleymani Eil Bakhtiari, Evaluation of physical, mechanical, and biodegradation of chitosan/graphene oxide composite as bone substitutes, Polym. Technol. Mater. 59 (2020) 430–440, https://doi.org/10.1080/25740881.2019.1653467.
[31] Y. Alikhasi, S. Ghadirian, N. Mohammadi, M. Shadkhast, S. Karbasi, Evaluation of the effects of chitosan nanoparticles on polyhydroxy butyrate electrospun scaffolds for cartilage tissue engineering applications, Int. J. Biol. Macromol. 249 (2023) 126064, https://doi.org/10.1016/j.ijbiomac.2023.126064.
[32] E.B. Toloue, S. Karbasi, H. Salehi, M. Rafienia, Potential of an electrospun composite scaffold of poly (3-hydroxybutyrate)-chitosan/alumina nanowires in bone tissue engineering applications, Mater. Sci. Eng. C 99 (2019) 1075–1091, https://doi.org/10.1016/j.msec.2019.02.062.
[33] S. Ghadirian, S. Karbasi, Evaluation of the effects of halloysite nanotube on polyhydroxybutyrate - chitosan electrospun scaffolds for cartilage tissue engineering applications, Int. J. Biol. Macromol. 233 (2023) 123651, https://doi.org/10.1016/j.ijbiomac.2023.123651.
[34] S. Keikhaei, Z. Mohammadalizadeh, S. Karbasi, A. Salimi, Evaluation of the effects of ß-tricalcium phosphate on physical, mechanical and biological properties of Poly (3-hydroxybutyrate)/chitosan electrospun scaffold for cartilage tissue engineering applications, Mat. Technol. 34 (10) (2019) 615–625, https://doi.org/10.1080/10667857.2019.1611053.
[35] E.S. Motiee, S. Karbasi, E. Bidram, M. Sheikholeslam, Investigation of physical, mechanical and biological properties of polyhydroxybutyrate-chitosan/graphene oxide nanocomposite scaffolds for bone tissue engineering applications, Int. J. Biol. Macromol. 247 (2023) 125593, https://doi.org/10.1016/j.ijbiomac.2023.125593.
[36] S. Karbasi, Z.M. Alizadeh, Effects of multi-wall carbon nanotubes on structural and mechanical properties of poly(3-hydroxybutyrate)/chitosan electrospun scaffolds for cartilage tissue engineering, Bull. Mater. Sci. 40 (2017) 1247–1253, https://doi.org/10.1007/s12034-017-1479-9.
[37] Z. Mohammadalizadeh, S. Karbasi, S. Arasteh, Physical, mechanical and biological evaluation of poly (3-hydroxybutyrate)-chitosan/MWNTs as a novel electrospun scaffold for cartilage tissue engineering applications, Polym. Technol. Mater. 59 (2020) 417–429, https://doi.org/10.1080/25740881.2019.1647244.
[38] M. Khoroushi, M.R. Foroughi, S. Karbasi, B. Hashemibeni, A.A. Khademi, Effect of Polyhydroxybutyrate/chitosan/bioglass nanofiber scaffold on proliferation and differentiation of stem cells from human exfoliated deciduous teeth into odontoblast-like cells, Mater. Sci. Eng. C 89 (2018) 128–139, https://doi.org/10.1016/j.msec.2018.03.028.
[39] M. Mohammadalipour, S. Karbasi, T. Behzad, Z. Mohammadalipour, M. Zamani, Effect of cellulose nanofibers on polyhydroxybutyrate electrospun scaffold for bone tissue engineering applications, Int. J. Biol. Macromol. 220 (2022) 1402–1414, https://doi.org/10.1016/j.ijbiomac.2022.09.118.
[40] S.B.A. Boraei, F. Eshghabadi, R. Hosseinpour, Y. Zare, M.T. Munir, K.Y. Rhee, Halloysite nanotubes in biomedical applications: recent approaches and future trends, Appl. Clay Sci. 253 (2024) 107346.
[41] A. Mitropoulou, D.N. Markatos, A. Dimopoulos, A. Marazioti, C.M. Mikelis, D. Mavrilas, Development and evaluation of biodegradable Core-Shell microfibrous and Nanofibrous scaffolds for tissue engineering applications, J. Mater. Sci. Mater. Med. 35 (2024), https://doi.org/10.1007/s10856-024-06777-z.
[42] N.K. Karamanos, A.D. Theocharis, Z. Piperigkou, D. Manou, A. Passi, S. S. Skandalis, D.H. Vynios, V. Orian-Rousseau, S. Ricard-Blum, C.E.H. Schmelzer, L. Duca, M. Durbeej, N.A. Afratis, L. Troeberg, M. Franchi, V. Masola, M. Onisto, A guide to the composition and functions of the extracellular matrix, FEBS J. 288 (2021) 6850–6912, https://doi.org/10.1111/febs.15776.
[43] P. Xu, R.K. Kankala, S. Wang, A. Chen, Decellularized extracellular matrix-based composite scaffolds for tissue engineering and regenerative medicine, Regen. Biomater. 11 (2024), https://doi.org/10.1093/rb/rbad107.
[44] S. Thakkar, C.A. Ghebes, M. Ahmed, C. Kelder, C.A. Van Blitterswijk, D. Saris, H. A.M. Fernandes, L. Moroni, Mesenchymal stromal cell-derived extracellular matrix influences gene expression of chondrocytes, Biofabrication 5 (2013), https://doi.org/10.1088/1758-5082/5/2/025003.
[45] E.A. Kiyotake, E.C. Beck, M.S. Detamore, Cartilage extracellular matrix as a biomaterial for cartilage regeneration, Ann. N. Y. Acad. Sci. 1383 (2016) 139–159, https://doi.org/10.1111/nyas.13278.
[46] I.-C. Lin, T.-J. Wang, C.-L. Wu, D.-H. Lu, Y.-R. Chen, K.-C. Yang, Chitosan-cartilage extracellular matrix hybrid scaffold induces chondrogenic differentiation to adipose-derived stem cells, Regen. Ther. 14 (2020) 238–244, https://doi.org/10.1016/j.reth.2020.03.014.
[47] B. Choi, S. Kim, B. Lin, B.M. Wu, M. Lee, Cartilaginous extracellular matrix-modified chitosan hydrogels for cartilage tissue engineering, ACS Appl. Mater. Interfaces 6 (2014) 20110–20121, https://doi.org/10.1021/am505723k.
[48] M. Asghari-Vostakolaei, H. Bahramian, S. Karbasi, M. Setayeshmehr, Effects of decellularized extracellular matrix on Polyhydroxybutyrate electrospun scaffolds for cartilage tissue engineering, Polym. Technol. Mater. 00 (2022) 1–19, https://doi.org/10.1080/25740881.2022.2150863.
[49] E. Masaeli, F. Karamali, S. Loghmani, M.B. Eslaminejad, M.H. Nasr-Esfahani, Bio-engineered electrospun nanofibrous membranes using cartilage extracellular matrix particles, J. Mater. Chem. B 5 (2017) 765–776, https://doi.org/10.1039/C6TB02015A.
[50] X. Zhang, Z. Deng, H. Wang, Z. Yang, W. Guo, Y. Li, D. Ma, C. Yu, Y. Zhang, Y. Jin, Expansion and delivery of human fibroblasts on micronized acellular dermal matrix for skin regeneration, Biomaterials 30 (2009) 2666–2674, https://doi.org/10.1016/j.biomaterials.2009.01.018.
[51] D.O. Freytes, J. Martin, S.S. Velankar, A.S. Lee, S.F. Badylak, Preparation and rheological characterization of a gel form of the porcine urinary bladder matrix, Biomaterials 29 (2008) 1630–1637.
[52] A. Honarvar, M. Setayeshmehr, S. Ghaedamini, L. Moroni, S. Karbasi, Chondrogenesis of mesenchymal stromal cells on the 3D printed polycaprolactone / fibrin / decellular cartilage matrix hybrid scaffolds in the presence of piascledine, J. Biomater. Sci. Polym. Ed. 35 (2024) 799–822, https://doi.org/10.1080/09205063.2024.2307752.
[53] R. Aslani, M. Mirzadeh, S.A. Poursamar, A.A. Rabiei, M. Setayeshmehr, Extracellular matrix coated three-dimensional-printed polycaprolactone scaffolds containing curcumin for cartilage tissue engineering applications, J. Bioact. Compat. Polym. (2024), https://doi.org/10.1177/08839115241260060.
[54] T.T.T. Nguyen, O.H. Chung, J.S. Park, Coaxial electrospun poly (lactic acid)/chitosan (core/shell) composite nanofibers and their antibacterial activity, Carbohydr. Polym. 86 (2011) 1799–1806.
[55] R. Murphy, A. Turcott, L. Banuelos, E. Dowey, B. Goodwin, K.O. Cardinal, Simpoly: a Matlab-based image analysis tool to measure electrospun polymer scaffold fiber diameter, Tissue Eng. Part C Methods 26 (2020) 628–636, https://doi.org/10.1089/ten.tec.2020.0304.
[56] R. Al-Gaashani, Y. Zakaria, I. Gladich, V. Kochkodan, J. Lawler, XPS, structural and antimicrobial studies of novel functionalized halloysite nanotubes, Sci. Rep. 12 (2022) 21633.
[57] S. Ghadirian, S. Karbasi, A.Z. Kharazi, M. Setayeshmehr, Evaluation of the effects of Halloysite nanotubes on physical, mechanical, and biological properties of Polyhydroxy butyrate electrospun scaffold for cartilage tissue engineering applications, J. Polym. Environ. (2023), https://doi.org/10.1007/s10924-023-03024-4.
[58] F. Porzucek, M. Mankowska, J.A. Semba, P. Cywoniuk, A. Augustyniak, A. M. Mleczko, A.M. Teixeira, P. Martins, A.A. Mieloch, J.D. Rybka, Development of

a porcine decellularized extracellular matrix (DECM) bioink for 3D bioprinting of meniscus tissue engineering: formulation, characterisation and biological evaluation, Virtual Phys. Prototyp. 19 (2024) 1–14, https://doi.org/10.1080/17452759.2024.2359620.
[59] M. Soleymani, E.-S. Motiee, S. Karbasi, A. Basiri, Evaluation of the effects of decellularized umbilical cord Wharton's jelly ECM on polyhydroxy butyrate electrospun scaffolds: a new strategy for cartilage tissue engineering, Mater. Today Chem. 39 (2024) 102145.
[60] Y. Lu, Y. Wang, H. Zhang, Z. Tang, X. Cui, X. Li, J. Liang, Q. Wang, Y. Fan, X. Zhang, Solubilized cartilage ECM facilitates the recruitment and Chondrogenesis of endogenous BMSCs in collagen scaffolds for enhancing microfracture treatment, ACS Appl. Mater. Interfaces (2021), https://doi.org/10.1021/acsami.1c07530.
[61] H. Zhang, C. Zhao, Y. Zhao, G. Tang, X. Yuan, Electrospinning of ultrafine core/shell fibers for biomedical applications, Sci. China Chem. 53 (2010) 1246–1254, https://doi.org/10.1007/s11426-010-3180-3.
[62] J.M. Anaya Mancipe, L.C. Boldrini Pereira, P.G. de Miranda Borchio, M.L. Dias, R. M. da Silva Moreira Thiré, Novel polycaprolactone (PCL)-type I collagen core-shell electrospun nanofibers for wound healing applications, J. Biomed. Mater. Res. - Part B Appl. Biomater. 111 (2023) 366–381, https://doi.org/10.1002/jbm.b.35156.
[63] K. Sun, Z.H. Li, Preparations, properties and applications of chitosan based nanofibers fabricated by electrospinning, Express Polym Lett 5 (2011) 342–361, https://doi.org/10.3144/expresspolymlett.2011.34.
[64] N. Bhattarai, D. Edmondson, O. Veiseh, F.A. Matsen, M. Zhang, Electrospun chitosan-based nanofibers and their cellular compatibility, Biomaterials 26 (2005) 6176–6184, https://doi.org/10.1016/j.biomaterials.2005.03.027.
[65] L. Ma, X. Shi, X. Zhang, L. Li, Electrospinning of polycaprolacton/chitosan core-shell nanofibers by a stable emulsion system, Colloids Surfaces A Physicochem. Eng. Asp. 583 (2019) 123956, https://doi.org/10.1016/j.colsurfa.2019.123956.
[66] S.C. Suner, A. Oral, Y. Yildirim, Design of Poly(lactic) acid/gelatin core-shell bicomponent systems as a potential wound dressing material, J. Mech. Behav. Biomed. Mater. 150 (2024) 106255, https://doi.org/10.1016/j.jmbbm.2023.106255.
[67] S. Asthana, P. Goyal, R. Dhar, U. K, N.B. Pampanaboina, J. Christakiran, S. S. Sagiri, M. Khanna, A. Samal, I. Banerjee, K. Pal, K. Pramanik, S.S. Ray, Evaluation extracellular matrix–chitosan composite films for wound healing application, J. Mater. Sci. Mater. Med. 26 (2015) 220, https://doi.org/10.1007/s10856-015-5551-y.
[68] S. Saeedi Garakani, M. Khanmohammadi, Z. Atoufi, S.K. Kamrava, M. Setayeshmehr, R. Alizadeh, F. Faghihi, Z. Bagher, S.M. Davachi, A. Abbaspourrad, Fabrication of chitosan/agarose scaffolds containing extracellular matrix for tissue engineering applications, Int. J. Biol. Macromol. 143 (2020) 533–545, https://doi.org/10.1016/j.ijbiomac.2019.12.040.
[69] J. Nie, Z. liang Wang, J. fu Li, Y. Gong, J. xing Sun, S. guang Yang, Interface hydrogen-bonded core-shell nanofibers by coaxial electrospinning, Chin. J. Polym. Sci. (Engl. Ed.) 35 (2017) 1001–1008, https://doi.org/10.1007/s10118-017-1984-8.
[70] S.K. Tiwari, S.S. Venkatraman, Importance of viscosity parameters in electrospinning: of monolithic and core–shell fibers, Mater. Sci. Eng. C 32 (2012) 1037–1042, https://doi.org/10.1016/j.msec.2012.02.019.
[71] S. Soliman, S. Sant, J.W. Nichol, M. Khabiry, E. Traversa, A. Khademhosseini, Controlling the porosity of fibrous scaffolds by modulating the fiber diameter and packing density, J. Biomed. Mater. Res. Part A. 96A (2011) 566–574, https://doi.org/10.1002/jbm.a.33010.
[72] A. Heidarkhan Tehrani, A. Zadhoush, S. Karbasi, H. Sadeghi-Aliabadi, Scaffold percolative efficiency: in vitro evaluation of the structural criterion for electrospun mats, J. Mater. Sci. Mater. Med. 21 (2010) 2989–2998, https://doi.org/10.1007/s10856-010-4149-7.
[73] A.S. Badami, M.R. Kreke, M.S. Thompson, J.S. Riffle, A.S. Goldstein, Effect of fiber diameter on spreading, proliferation, and differentiation of osteoblastic cells on electrospun poly(lactic acid) substrates, Biomaterials 27 (2006) 596–606, https://doi.org/10.1016/j.biomaterials.2005.05.084.
[74] A. Saberi, E. Khodaverdi, H. Kamali, J. Movaffagh, M. Mohammadi, D. Yari, A. Moradi, F. Hadizadeh, Fabrication and characterization of biomimetic electrospun cartilage Decellularized matrix (CDM)/chitosan nanofiber hybrid for tissue engineering applications: box-Behnken Design for Optimization, J. Polym. Environ. 32 (2024) 1573–1592.
[75] J.Y. Lim, H.J. Donahue, Cell sensing and response to micro- and nanostructured surfaces produced by chemical and topographic patterning, Tissue Eng. 13 (2007) 1547e1560, https://doi.org/10.1089/ten.2006.0154.
[76] M.M. Stevens, J.H. George, Exploring and engineering the cell surface interface, Science 310 (2005) 1135–1138, https://doi.org/10.1126/science.1106587.
[77] L. Chou, J.D. Firth, V.-J. Uitto, D.M. Brunette, Substratum surface topography alters cell shape and regulates fibronectin mRNA level, mRNA stability, secretion and assembly in human fibroblasts, J. Cell Sci. 108 (1995) 1563–1573, https://doi.org/10.1242/jcs.108.4.1563.
[78] M.J. Dalby, Topographically induced direct cell mechanotransduction, Med. Eng. Phys. 27 (2005) 730–742, https://doi.org/10.1016/j.medengphy.2005.04.005.
[79] A.F. Peixoto, A.C. Fernandes, C. Pereira, J. Pires, C. Freire, Physicochemical characterization of organosilylated halloysite clay nanotubes, Microporous Mesoporous Mater. 219 (2016) 145–154, https://doi.org/10.1016/j.micromeso.2015.08.002.
[80] H. Alamri, I.M. Low, Microstructural, mechanical, and thermal characteristics of recycled cellulose fiber-halloysite-epoxy hybrid nanocomposites, Polym. Compos. 33 (2012) 589–600.
[81] K. Govindasamy, N.A. Dahlan, P. Janarthanan, K.L. Goh, S.P. Chai, P. Pasbakhsh, Electrospun chitosan/polyethylene-oxide (PEO)/halloysites (HAL) membranes for bone regeneration applications, Appl. Clay Sci. 190 (2020) 105601, https://doi.org/10.1016/j.clay.2020.105601.
[82] M. Liu, C. Wu, Y. Jiao, S. Xiong, C. Zhou, Chitosan-halloysite nanotubes nanocomposite scaffolds for tissue engineering, J. Mater. Chem. B 1 (2013) 2078–2089, https://doi.org/10.1039/c3tb20084a.
[83] L.S. Shibryaeva, O.V. Shatalova, A.V. Krivandin, Y.V. Tertyshnaya, Y.V. Solovova, Specific structural features of crystalline regions in biodegradable composites of poly-3-hydroxybutyrate with chitosan, Russ. J. Appl. Chem. 90 (2017) 1443–1453, https://doi.org/10.1134/S1070427217090117.
[84] B. de Campos Vidal, M.L.S. Mello, FT-IR microspectroscopy of rat ear cartilage, PloS One 11 (2016) 1–13, https://doi.org/10.1371/journal.pone.0151989.
[85] Z. Chen, X. Mo, F. Qing, Electrospinning of collagen-chitosan complex, Mater. Lett. 61 (2007) 3490–3494, https://doi.org/10.1016/j.matlet.2006.11.104.
[86] L. Rieppo, T. Närhi, H.J. Helminen, J.S. Jurvelin, S. Saarakkala, J. Rieppo, Infrared spectroscopic analysis of human and bovine articular cartilage proteoglycans using carbohydrate peak or its second derivative, J. Biomed. Opt. 18 (2013) 097006, https://doi.org/10.1117/1.jbo.18.9.097006.
[87] Z. Movasaghi, S. Rehman, I.U. Rehman, Fourier transform infrared (FTIR) spectroscopy of biological tissues, Appl. Spectrosc. Rev. 43 (2008) 134–179, https://doi.org/10.1080/05704920701829043.
[88] M.S. Bergholt, A. Serio, M.B. Albro, Raman spectroscopy: guiding light for the extracellular matrix, Front. Bioeng. Biotechnol. 7 (2019) 1–16, https://doi.org/10.3389/fbioe.2019.00303.
[89] R. Nirmala, B.W. Il, R. Navamathavan, M.H. El-newehy, H.Y. Kim, Preparation and characterizations of anisotropic chitosan nanofibers via electrospinning, Macromol. Res. 19 (2011) 345–350, https://doi.org/10.1007/s13233-011-0402-2.
[90] A. Zając, J. Hanuza, M. Wandas, L. Dymińska, Determination of N-acetylation degree in chitosan using Raman spectroscopy, Spectrochim. Acta A Mol. Biomol. Spectrosc. 134 (2015) 114–120, https://doi.org/10.1016/j.saa.2014.06.071.
[91] M. Ioelovich, Crystallinity and hydrophility of chitin and chitosan, J. Chem. 3 (2014) 7–14.
[92] B. Feng, T. Ji, X. Wang, W. Fu, L. Ye, H. Zhang, F. Li, Engineering cartilage tissue based on cartilage-derived extracellular matrix cECM/PCL hybrid nanofibrous scaffold, Mater. Des. 193 (2020) 108773, https://doi.org/10.1016/j.matdes.2020.108773.
[93] Z. Chen, X. Mo, C. He, H. Wang, Intermolecular interactions in electrospun collagen–chitosan complex nanofibers, Carbohydr. Polym. 72 (2008) 410–418, https://doi.org/10.1016/j.carbpol.2007.09.018.
[94] J. Xu, H. Fang, S. Zheng, L. Li, Z. Jiao, H. Wang, Y. Nie, T. Liu, K. Song, A biological functional hybrid scaffold based on decellularized extracellular matrix/gelatin/chitosan with high biocompatibility and antibacterial activity for skin tissue engineering, Int. J. Biol. Macromol. 187 (2021) 840–849, https://doi.org/10.1016/j.ijbiomac.2021.07.162.
[95] R. Bual, H. Kimura, Y. Ikegami, N. Shirakigawa, H. Ijima, Fabrication of liver-derived extracellular matrix nanofibers and functional evaluation in in vitro culture using primary hepatocytes, Materialia 4 (2018) 518–528, https://doi.org/10.1016/j.mtla.2018.11.014.
[96] B. Kaczmarek, A. Sionkowska, J. Skopinska-Wisniewska, Influence of glycosaminoglycans on the properties of thin films based on chitosan/collagen blends, J. Mech. Behav. Biomed. Mater. 80 (2018) 189–193, https://doi.org/10.1016/j.jmbbm.2018.02.006.
[97] J. Elango, J. Zhang, B. Bao, K. Palaniyandi, S. Wang, W. Wu, J. Shakila, Rheological, biocompatibility and osteogenesis assessment of fish collagen scaffold for bone tissue engineering, Int. J. Biol. Macromol. 91 (2016) 51–59. https://doi.org/10.1016/j.ijbiomac.2016.05.067.
[98] D.P. Dowling, I.S. Miller, M. Ardhaoui, W.M. Gallagher, Effect of surface wettability and topography on the adhesion of osteosarcoma cells on plasma-modified polystyrene, J. Biomater. Appl. 26 (2011) 327–347, https://doi.org/10.1177/0885328210372148.
[99] S. Ghasemi, A. Alibabaie, R. Saberi, M. Esmaeili, D. Semnani, S. Karbasi, Evaluation of the effects of zein incorporation on physical, mechanical, and biological properties of polyhydroxybutyrate electrospun scaffold for bone tissue engineering applications, Int. J. Biol. Macromol. 253 (2023) 126843, https://doi.org/10.1016/j.ijbiomac.2023.126843.
[100] E.Y. Salinas, J.C. Hu, K. Athanasiou, A guide for using mechanical stimulation to enhance tissue-engineered articular cartilage properties, Tissue Eng. - Part B Rev. 24 (2018) 345–358, https://doi.org/10.1089/ten.teb.2018.0006.
[101] N. Petitjean, P. Canadas, P. Royer, D. Noël, S. Le Floc'h, Cartilage biomechanics: from the basic facts to the challenges of tissue engineering, J. Biomed. Mater. Res. - Part A. 111 (2023) 1067–1089, https://doi.org/10.1002/jbm.a.37478.
[102] R.M. Raftery, B. Woods, A.L.P. Marques, J. Moreira-Silva, T.H. Silva, S.-A. Cryan, R.L. Reis, F.J. O'Brien, Multifunctional biomaterials from the sea: assessing the effects of chitosan incorporation into collagen scaffolds on mechanical and biological functionality, Acta Biomater. 43 (2016) 160–169, https://doi.org/10.1016/j.actbio.2016.07.009.
[103] M.A. Boos, S.R. Lamandé, K.S. Stok, Multiscale strain transfer in cartilage, front. Cell, Dev. Biol. 10 (2022) 1–12, https://doi.org/10.3389/fcell.2022.795522.
[104] Y. Tang, L. Chen, K. Zhao, Z. Wu, Y. Wang, Q. Tan, Fabrication of PLGA / HA (core) -collagen / amoxicillin (shell) nano fi ber membranes through coaxial electrospinning for guided tissue regeneration, Compos. Sci. Technol. 125 (2016) 100–107, https://doi.org/10.1016/j.compscitech.2016.02.005.
[105] Y.A. Amnieh, S. Karbasi, S.H. Dehkordi, M. Shadkhast, A. Basiri, Evaluation of the Effects of Decellularized Wharton Jelly Nanoparticles on Polyhydroxy Butyrate-

Chitosan Electrospun Scaffolds for Cartilage Tissue Engineering Applications, J. Polym. Environ. 33 (2025) 545–569, https://doi.org/10.1007/s10924-024-03385-4.
[106] J.E. Reing, L. Zhang, J. Myers-Irvin, K.E. Cordero, D.O. Freytes, E. Heber-Katz, K. Bedelbaeva, D. McIntosh, A. Dewilde, S.J. Braunhut, Degradation products of extracellular matrix affect cell migration and proliferation, Tissue Eng. Part A 15 (2009) 605–614.
[107] M. Mohammadalipour, M. Asadolahi, Z. Mohammadalipour, T. Behzad, S. Karbasi, Plasma surface modification of electrospun polyhydroxybutyrate (PHB) nanofibers to investigate their performance in bone tissue engineering, Int. J. Biol. Macromol. 230 (2023) 123167, https://doi.org/10.1016/j.ijbiomac.2023.123167.
[108] W.-J. Li, Y.J. Jiang, R.S. Tuan, Chondrocyte phenotype in engineered fibrous matrix is regulated by fiber size, Tissue Eng. 12 (2006) 1775–1785.
[109] T.M. Ulrich Meyer, Jörg Handschel, Hans Peter Wiesmann, Fundamentals of Tissue Engineering and Regenerative Medicine (2009), https://doi.org/10.1007/978-3-540-77755-7.
[110] S. Ravindran, M. Kotecha, C.-C. Huang, A. Ye, P. Pothirajan, Z. Yin, R. Magin, A. George, Biological and MRI characterization of biomimetic ECM scaffolds for cartilage tissue regeneration, Biomaterials 71 (2015) 58–70, https://doi.org/10.1016/j.biomaterials.2015.08.030.
[111] T. Xiao, W. Guo, M. Chen, C. Hao, S. Gao, J. Huang, Z. Yuan, Y. Zhang, M. Wang, P. Li, J. Peng, A. Wang, Y. Wang, X. Sui, L. Zhang, W. Xu, S. Lu, H. Yin, J. Yang, S. Liu, Q. Guo, Fabrication and in vitro study of tissue-engineered cartilage scaffold derived from Wharton's jelly extracellular matrix, Biomed. Res. Int. 2017 (2017), https://doi.org/10.1155/2017/5839071.
[112] F. Otto, DAPI Staining of Fixed Cells for High-Resolution Flow Cytometry of Nuclear DNA, Methods Cell Biol., Elsevier, in, 1990, pp. 105–110.
[113] C.H. Chang, C.C. Chen, C.H. Liao, F.H. Lin, Y.M. Hsu, H.W. Fang, Human acellular cartilage matrix powders as a biological scaffold for cartilage tissue engineering with synovium-derived mesenchymal stem cells, J. Biomed. Mater. Res. - Part A. 102 (2014) 2248–2257, https://doi.org/10.1002/jbm.a.34897.
[114] T.E. Hardingham, R.A. Oldershaw, S.R. Tew, Cartilage, SOX9 and notch signals in chondrogenesis, J. Anat. 209 (2006) 469–480, https://doi.org/10.1111/j.1469-7580.2006.00630.x.
[115] Y. Li, W. Chen, Y. Dai, Y. Huang, Z. Chen, T. Xi, Z. Zhou, H. Liu, Decellularized sturgeon cartilage extracellular matrix scaffold inhibits chondrocyte hypertrophy in vitro and in vivo, J. Tissue Eng. Regen. Med. 15 (2021) 732–744, https://doi.org/10.1002/term.3222.
[116] M.R. Foroughi, S. Karbasi, R. Ebrahimi-Kahrizsangi, Physical and mechanical properties of a poly-3-hydroxybutyrate-coated nanocrystalline hydroxyapatite scaffold for bone tissue engineering, J. Porous Mat. 19 (2012) 667–675, https://doi.org/10.1007/s10934-011-9518-1.